
Sediment routing from shelf to basin floor in the Quaternary Golo System of Eastern Corsica, France, western Mediterranean Sea

Sweet Michael L. ^{1,*}, Gaillot Gwladys T. ², Jouet Gwenael ³, Rittenour Tammy M. ⁴, Toucanne Samuel ³, Marsset Tania ³, Blum Michael D. ⁵

¹ ExxonMobil Upstream Research Company, 22777 Springwoods Village Parkway, Spring, Texas 77389, USA

² ExxonMobil Upstream Business Development Company, USA

³ Institute Français de Recherche L'Exploitation de la Mer, Géosciences Marines, F-29280 Plouzané, France

⁴ Department of Geology, Utah State University, 4505 Old Main Hall, Logan, Utah 84322, USA

⁵ Department of Geology, 1475 Jayhawk Blvd., University of Kansas, Kansas 66045, USA

* Corresponding author : Michael L. Sweet, email address : mlsweet@swbell.net

Abstract :

How and when sediment moves from shallow marine to deep-water environments is an important and poorly understood control on basin-scale sediment dispersal patterns, the evolution of continental margins, and hydrocarbon exploration in deep-water basins. The Golo River (Eastern Corsica, France), its delta, canyons, and fans provide a unique opportunity to study sediment routing from source to sink in a relatively compact depositional system. We studied this system using an array of high-frequency seismic data, multi-beam bathymetry, and five cores for lithology and age control.

Movement of sediment to deep water was controlled by interactions between the Golo River, the Golo Delta, and shelf-penetrating submarine canyons. Sediment moved to deep water when lobes of the Golo Delta prograded to the heads of these canyons, or when the Golo River itself flowed directly into one of them. Sand accumulated in canyons, deep-water channels, and submarine fans during glacial periods of low sea level, while mud was deposited throughout the slope, in the relatively short reach of leveed-confined channels, and in the mud-rich fringes around the sandy fans. During interglacial periods of high sea level, the basin was blanketed by mud-rich deposits up to 10 m thick interbedded with distinctive carbonate-rich sediments. Deposition rates in the basin ranged from 0.07 m/ka to 0.59 m/ka over the last 450 ka. Mud deposition rates remained relatively constant at ≤ 0.16 m/ka during all time periods, while sand deposition only happened during glacial periods of low sea level with an average rate of 0.24 m/ka.

In addition to sea-level controls on sediment delivery, avulsions of the Golo River and its deltaic lobes preferentially routed sediment down either the North or South Golo canyons. Thus, while the larger, sequencescale architecture of the basin is controlled by allogenic sea level forcing, millennial-scale autogenic processes operating on the shelf and in deep water shaped the distribution of sand and mud, and the internal geometry of the deltas and submarine fans that they fed. While some aspects of the Golo system are characteristic of steep, tectonically active margins, others such as the nature of connections

between rivers and shelf-penetrating submarine canyons are observed in most margins with active submarine fans regardless of their tectonic setting.

40 INTRODUCTION

41 New insights into deep-water depositional systems are coming from a growing body of
42 literature that describes the geometry and facies distribution observed from high-resolution
43 seismic, multi-beam bathymetry, and core data in Quaternary deep-water systems (e.g.,
44 Babonneau et al., 2002; Deptuk et al., 2008; Maier et al., 2012; Sylvester, 2012; Paull et al.,
45 2013; Jobe et al., 2015; Picot et al., 2016). These studies provide a richer understanding of three-
46 dimensional facies geometries relative to outcrops and enable deep-water systems to be more
47 clearly placed in the context of external controls such as climate, tectonic setting, sea level
48 change, and basin morphology as well as inherent autogenic processes.

49 This study examines the Golo system of eastern offshore Corsica using a relatively
50 closely spaced grid of high-resolution, multi-channel sparker seismic data (400 to 800 m

51 spacing), multi-beam bathymetry, and lithology and chronological constraints from 5 long (up to
52 126 m) cores to document facies distribution and sediment flux through a Quaternary system
53 from deltas to slope canyons and to submarine fans (Figures 1 and 2). The Corsica Trough was
54 chosen for this study because it is a compact basin where seismic data could be acquired across a
55 range of depositional environments from deltaic to deep-water fans in a depositional system that
56 was constrained by previous work. These seismic data allowed us to map sediment volumes in
57 5 depositional sequences spanning the last ~450 ka. We utilized a variety of geochronological
58 tools (^{14}C , Optically Stimulated Luminescence (OSL), and $\delta^{18}\text{O}$ curves) to date the timing of
59 sediment flux into the basin and to determine rates of sedimentation through multiple sea level
60 cycles.

61 The objectives of this study are:

- 62 1) Map and interpret the shape, distribution, and origin of sedimentary bodies.
- 63 2) Quantify how the mud and sand fractions of sediment loads are partitioned between shelf,
64 slope and deep-water environments.
- 65 3) Quantify how and when sediment moved from the shelf into deep water.
- 66 4) Examine the external controls on deep-water-fan growth.

67

68 **Corsica and the East Corsica Basin**

69 Corsica is a mountainous island in the western Mediterranean Sea 85 km wide and 180
70 km long, with the highest peaks rising to an elevation of over 2700 m. On the western margin of
71 the island the mountains come down to the coast and there is only a narrow coastal plain (Figure
72 1). Offshore, water depths rapidly fall off to over 2500 m. In contrast, the eastern margin of the
73 island has a wider coastal plain (about 15 km) that represents the alluvial plains and deltas of the

74 Golo and Tavignano rivers (Figure 1). These rivers are short, high-gradient streams with flashy
75 discharges and high sediment yields that are capable of generating hyperpycnal flows when in
76 flood stage (Mulder and Maneaux, 1999). In our study area, sediment is primarily delivered by
77 the Golo River (Figure 1).

78 The present-day shelf ranges in width from 4 to 9 km within the limits of our study area,
79 and the strong, north-directed Tyrrhenian Current sweeps it clear of fine-grained Holocene
80 sediment (Astraldi and Gasparini, 1992; Pluquet, 2006). The shelf-slope break occurs at -120 m.
81 The continental slope leading to the south-plunging Corsica Trough is narrow with a gradient of
82 3 to 5 degrees, and water depths of over 900 m (Figure 1). The eastern side of the Corsica
83 Trough is formed by a structural high, the Pianosa Ridge, which is steeper than the Corsica side
84 of the Trough. The slope here dips westward at 3.5 to 7.5 degrees (Deptuck et al., 2008). Most of
85 the Pianosa Ridge is submerged with the small island of Elba being the largest nearby landmass
86 (Figure 1). While there are no canyons on the eastern side of the basin, seismic mapping by
87 Miramontes et al (2016a and b) shows evidence for slumps and slides, as well as extensive
88 contourite deposits. Our seismic mapping, discussed below, suggests there is little sediment
89 contribution from the Pianosa Ridge to the Corsica Trough, with the exception of some localized
90 debris flow deposits.

91 More broadly, the island of Corsica and the adjacent Corsica Trough are part of a backarc
92 basin associated with the early Miocene opening of the Tyrrhenian Sea (Jolivet et al., 1998). The
93 basin contains up to 10 km of Pleistocene to Miocene-age syn-rift and post-rift sediments
94 (Mauffert et al, 1999). The other major factor that affected the Neogene configuration of this
95 area was the Miocene evaporation of the Mediterranean which caused a dramatic regrading of
96 rivers and incision of canyons all along the Mediterranean coastline with Corsica being no

97 exception (Hsu, 1973; Ryan, 2009). The Messinian erosion surface can be seen on some of our
98 seismic data, but it is well below the maximum depth of investigation for this study.

99

100 **Previous Work on Golo/Corsica Basin**

101 The first seismic data shot across the Corsica Trough (Gabin, 1972) showed the general
102 configuration of the basin. Seismic and piston-core data published by Stanley et al. (1980) more
103 thoroughly characterized the Golo fans and provided insight into the near-surface Quaternary
104 sediment types and their ages. Bellaiche et al. (1994) published a detailed bathymetric map of the
105 area covering the North and South Golo canyons and the North and South Golo fans. Gervais et
106 al. (2004) and Gervais et al. (2006) mapped major depositional elements of the North and South
107 Golo canyons, as well as their associated channels, levees and lobe complexes from >1000 km of
108 sparker seismic data and 35 shallow cores. In addition, they provided a stratigraphic framework
109 for the last 40 ka. Deptuck et al. (2008) focused on the youngest deposits, primarily from the
110 submarine fans, using 1300 km of ultra-high resolution, deep-towed seismic boomer profiles.

111 Sømme et al. (2011) took a source-to-sink approach to the Golo system. They mapped
112 and dated the Upper Quaternary onshore deposits of the Golo River, calculated sediment fluxes
113 and used the stratigraphic framework of Deptuck et al. (2008) to analyze the controls on
114 sediment routing for the last 60 ka. Their study interpreted a nonlinear relationship between
115 onshore and offshore depositional environments with potential temporary storage and release of
116 sediment on the shelf. Deptuck et al. (2008) and Sømme et al. (2011) based their sediment flux
117 calculations on an age model based on seismic mapping calibrated to ¹⁴C ages from shallow
118 cores. Calves et al. (2013) pursued a similar source-to-sink analysis using very high-resolution
119 sub-bottom profiler and high-resolution sparker data. Their age model was based largely on

120 comparison of $\delta^{18}\text{O}$ and XRF-Ca intensity curves with global standards, and resulted in an age
121 model with older maximum ages (120 ka with up to 18 ka discrepancy) than the age model that
122 Deptuck et al. (2008) and Sømme et al. (2011) had used. With their method, Calves et al. (2013)
123 were able to provide age estimates for a slightly deeper portion of the fan, which allowed them to
124 run a source-to-sink analysis for the last 130 ka (i.e., over a full sea-level cycle). Calves et al.
125 (2013) highlighted a potential mismatch between the volume of sediments deposited offshore
126 and the predicted denudation rates from long-term averages. Toucanne et al. (2015) used the 126
127 m-long GDEC-4 core to provide a chronostratigraphic framework for the East Corsica margin
128 over the last ca. 450 ka, calibrated to seismic data. They interpreted their continuous, high-
129 resolution paleo-climatic record to reveal a close coupling between river runoff and glacial-
130 interglacial climate changes. Forzoni et al. (2015) studied sediment fluxes in the Golo River
131 drainage using OSL dating and numerical models compared to the sediment yield derived from
132 volumes and ages in the submarine fans from both Sømme et al. (2011) and Calves et al. (2013).
133 They interpreted mismatches to represent episodes of sediment storage within the catchment, and
134 lag times in sediment transport from the catchment area, as controlled by climate, sea-level
135 changes and local geomorphic thresholds. Miramontes et al. (2016b) related geostrophic
136 circulation through the Corsica Trough to the deposition of thick drift deposits along the eastern
137 margin of the trough.

138

139 **METHODS AND DATA**

140 **Seismic Data and Seismic Interpretation**

141 Seismic and bathymetric data were gathered in June of 2008 by the IFREMER research
142 vessel *Le Suroît*, as part of a joint research consortia between IFREMER, ExxonMobil and Total.

143 *Le Suroît* acquired 2950 km of multi-channel, sparker seismic data, referred to herein as the
144 Sigolo survey (Savoie, 2008), along with very high-resolution, sub-bottom profiler (CHIRP
145 mode) seismic data (Figure 2). Seismic and bathymetry data could only be acquired for that part
146 of the outer and middle shelf where water depths exceeded 30 m due to the draft of the *Le Suroît*.

147 Sigolo data were post-stack time-migrated and have a frequency content ranging from
148 130 to 750 Hz with a vertical resolution of 2 to 4 m. Line spacing was on a variable 800 m to 400
149 m grid, with more closely spaced lines acquired in the vicinity of the Golo canyons and in the
150 channel to lobe transition of the South Golo Fan (Figure 2). Seismic data were reprocessed after
151 the cruise to enhance imaging below the modern-day continental shelf and reduce the impact of
152 multiples. Wells were tied to the reprocessed seismic data using a constant velocity of 1600 m/s
153 below the mudline for the time/depth conversion. This velocity produced a good tie between
154 marls observed in core and high amplitude seismic reflections observed in the seismic data over
155 the basin. This character tie is more uncertain on the shelf where sediments are uniformly sandy
156 and could have higher seismic velocities due to compaction and cementation.

157 Seismic interpretation was done on a workstation using Petrel™ software. While there is
158 some controversy about how apply sequence stratigraphic techniques to mapping deep water
159 deposits (i.e., Neal and Abreu, 2009; Catuneanu, 2019), the following approach helped us to
160 interpret these data. We first looked for extensive surfaces that showed stratal terminations
161 (downlap, truncation and onlap). Following Mitchum (1985) downlap surfaces that could be
162 correlated across the study area are interpreted to represent submarine fan deposits resting on a
163 sequence boundary. Our definition of sequence boundaries follows Posamentier and Vail (1988).
164 We then identified the first basin-wide, high-amplitude, continuous seismic reflection that draped
165 the underlying stratigraphy (Figure 3). These surfaces were termed flooding surfaces. Surfaces

166 are assigned numbers, with the lowest numbers being the oldest, and we use the prefixes FS for
167 flooding surfaces and SB for sequence boundaries. To begin mapping, a series of looped and tied
168 seismic sections were constructed, starting in the deep basin. In some cases, reflections mapped
169 in the deep basin could be traced up the slope and onto the shelf, but many are lost due to
170 thinning or onlap in the upper slope. Furthermore, submarine canyons on the slope and the larger
171 submarine channels are a challenge to correlate across. In most cases it is impossible to
172 accurately correlate seismic events within the channel-fill deposits to a reflection outside the
173 channel or canyon because of the chaotic character of the seismic facies in the channel or
174 canyon. However, by tracing lines around the canyons it is possible to identify the same
175 reflection on both sides of the canyon and in that way develop a consistent stratigraphic
176 framework. We used these basin-wide surfaces to define depositional sequences bounded at the
177 base and top by sequence boundaries. In terms of mapping and understanding the distribution of
178 lithofacies we found it more useful to map systems tracts (Posamentier et al, 1988) than
179 sequences. The lowstand systems tract being defined by sediments between the sequence
180 boundary and the flooding surface (Van Wagoner et al., 1990). As we were not able to
181 consistently map the maximum flooding surface that separates the highstand from transgressive
182 systems tracts we lumped them together (i.e., the sediments between the flooding surface and the
183 overlying sequence boundary) for mapping purposes.

184 The approach of identifying surfaces marked by downlap, onlap, reflection terminations
185 and draping high-amplitude continuous seismic facies was applied sequentially to smaller and
186 smaller scale stratigraphic units. However, our more detailed mapping was restricted to the
187 deep-water basin due to the numerous multiples that underlie the shelf part of the succession, and
188 was performed at finer stratigraphic levels only in the youngest shelf deposits.

189

190 **Core Data**

191 In September 2009 a coring program, the Golodrill survey, was undertaken in
192 collaboration with IFREMER, Total, ExxonMobil and Fugro N. V. using the Fugro drillship *R/V*
193 *Bavenit* (Jouet, 2018). Five cores ranging in length from 65 to 126 m were collected on a shelf-
194 to-basin transect along the South Golo Canyon and Fan (Figure 2). Overall the coring program
195 was extremely successful. High recoveries were expected in fine-grained intervals, yet they
196 remained high within the sand- and gravel-rich intervals as well, such that total recovery ranged
197 from 75 to 93% (Table 1).

198 Cores were analyzed and described at IFREMER's lab in Brest, France where measurements
199 were made of total natural gamma ray radioactivity, laser particle size analysis as well as
200 calcimetry. Oxygen and carbon isotopes from benthic and planktic foraminifera were done at the
201 LSCE (Toucanne et al., 2015). Cores were also sampled for Optically Stimulated Luminescence
202 (OSL) and ¹⁴C dating.

203

204 ***Lithofacies from core***

205 Cores GDEC-1 and GDEC-3 were collected on the shelf to obtain data on the lithology
206 and age of shelf deposits. GDEC-1 was drilled in 116 m of water on seismic line Sigolo-034b
207 near the shelf-slope break where initial interpretation suggested the occurrence of delta lobes
208 attached to the canyon head (Figures 2 and Figure 4). GDEC-1 penetrated 75.2 m below the sea
209 floor (mbsf; Table 1), and encountered a range of grain sizes from silt and clay to gravel. The
210 lower 18 m is composed of gravel with carbonate cemented intervals, whereas the interval from
211 57-22 mbsf is dominated by interbedded fine to medium sand and silty clay. A sharp-based,

212 fining-upward unit composed of gravel at the base and silty-clay at the top occurred between 22
213 mbsf and 11 mbsf, and the upper 11 m is comprised of interbedded medium to coarse sand and
214 silty clay (Figure 5). GDEC-3 was drilled in 68 m of water at the intersection of seismic lines
215 Sigolo-034b and Sigolo-066 where initial interpretations suggested the presence of an isolated
216 delta lobe overlying the fill of a paleo-incised valley (Figures 2 and 4). GDEC-3 penetrated to a
217 depth of 64.8 mbsf (Table 1), where carbonate-cemented coarse sand is encountered (Figure 5).
218 Most of the cored interval consists of very fine to coarse sand. From 38 mbsf to the surface there
219 is an overall upward coarsening, starting in silt and ending in coarse sand at the sea floor. A thick
220 conglomerate was found at 11 m. Based on their location, seismic and core facies, GEDEC-1 and
221 GDEC-3 are interpreted to represent the deposits of prograding delta lobes and paleo-valley fills.

222 GDEC-4 was drilled on the mid to lower slope, in 491 m of water to a depth of 125.7
223 mbsf at the intersection of seismic lines Sigolo-085 and Sigolo-036 (Figure 6). The objective was
224 to sample facies well removed from the submarine canyons in an area of relatively slow and
225 continuous deposition to development a detailed $\delta^{18}\text{O}$ record that could be used for dating (see
226 Toucanne et al., 2015). Aside from a few thin silt beds the core is primarily composed of silty
227 clay and carbonate-rich silty clay, and included 9 marl layers that ranged in thickness from 1 to 8
228 m (Figure 5).

229 GDEC-6 and GDEC-8 were drilled on the submarine fan at depths of 826 m and 631 m
230 respectively. GDEC-6 was collected at the intersection of the Sigolo-058 and Sigolo-004
231 seismic lines, and drilled to a depth 80.2 mbsf (Figures 2 and 7). This core was collected where
232 seismic facies suggested the presence of sand-rich, lobe-margin deposits within two adjacent
233 lobes of the South Golo Fan, high-amplitude continuous reflections between them that were most
234 likely muds, and underlying high-amplitude continuous seismic facies that we hoped to use for

235 age control. The upper 50 m of the core is very sand-rich with grains of up to granule size. These
236 sands show normal grading and other sedimentary structures consistent with deposition from
237 turbidity currents. Unfortunately, due to time constraints the core could not be drilled deep
238 enough to encounter the high-amplitude continuous seismic facies as planned, although a thick
239 section of shale was recovered from 50 mbsf to 80 mbsf. This interval contained 3 marls ranging
240 from 0.5 to 1.5 m in thickness. GDEC-8 was drilled at the crossing of seismic lines Sigolo-048
241 and Sigolo-007 to a depth of 108.8 mbsf (Figure 2). The drilling objectives of this location were
242 to sample a proximal levee visible on bathymetric data, as well seismic facies interpreted as a
243 channel-lobe transition (Figure 8). Core facies and gamma-ray data show that the proximal levee
244 is muddier than expected, with slightly more silty layers at its base. Channel-lobe transition
245 deposits consists largely of coarse sand and gravel interbedded with carbonate-rich draping muds
246 (Figure 5). These sands show normal grading and other sedimentary structures consistent with
247 deposition from turbidity currents

248

249 ***Chronological Control***

250 We sampled cores for ^{14}C and OSL dating, and oxygen isotope analyses. Benthic
251 foraminifera and ostracod assemblages described from the GDEC-4 core, with results reported in
252 Minto'o et al. (2016).

253 Seventy samples for AMS radiocarbon dating were obtained from macrofossils (*Pecten*
254 and other bivalves, *Turritella* and other gastropods), woody material and foraminifera in the 5
255 cores, and were used to build our age model for the last 40 ka (Figure 5, Appendix 1). Samples
256 were analyzed by the Poznań Radiocarbon Laboratory, and lab results were corrected for a
257 marine reservoir effect of 400 yrs, except for those from the period 15-17 ka, for which a

258 correction of 800 yrs was applied (Siani et al., 2001). Radiocarbon ages were calibrated to
259 calendar years using CALIB Rev 7.0.0 (Stuiver and Reimer, 1993) and the IntCal13 calibration
260 curve (Reimer et al., 2009).

261 Twenty-two samples were collected for OSL dating from sands in the GDEC-1, GDEC-3,
262 GDEC- 6 and GDEC-8 cores (Appendix 2). Although widely used in fluvial and other sand-
263 dominated environments on land, OSL techniques have rarely been applied to dating deep water
264 deposits. We found that this technique gave excellent results and allowed direct dating of sands
265 as old as 127 ka. Sample analyses were performed in the Utah State University (USU) OSL Lab.
266 All samples were opened and processed under dim amber safelight conditions within the lab.
267 Sample processing followed standard procedures involving sieving, gravity separation and acid
268 treatments with HCl and HF to isolate the quartz component of a narrow grain-size range,
269 usually 90-150 μm . The purity of the samples was checked by measurement with infra-red
270 stimulation to detect the presence of feldspar. Sample processing procedures follow those
271 outlined in Aitken (1998) and described in Rittenour et al. (2003, 2005). The USU lab follows
272 the latest single-aliquot regenerative-dose (SAR) procedures for dating quartz sand (Murray and
273 Wintle 2000, 2003; Wintle and Murray 2006).

274 Stable carbon and oxygen isotopes were measured from planktic and benthic
275 foraminifera. $^{18}\text{O}/^{16}\text{O}$ and $^{13}\text{C}/^{12}\text{C}$ ratios ($\delta^{18}\text{O}$ and $\delta^{13}\text{C}$ respectively, expressed in ‰ versus
276 Vienna Pee-Dee Belemnite, VPDB) were measured at LSCE (Gif-sur-Yvette, France) on
277 Finnigan $\Delta+$, and OPTIMA and Elementar Isoprime GV mass spectrometers. VPDB is defined
278 with respect to NBS-19 calcite standard ($\delta^{18}\text{O} = -2.20\text{‰}$ and $\delta^{13}\text{C} = +1.95\text{‰}$). The mean
279 external reproducibility (1σ) of carbonate standards is $\pm 0.05\text{‰}$ for $\delta^{18}\text{O}$ and $\pm 0.03\text{‰}$ for $\delta^{13}\text{C}$.
280 Measured NBS-19 $\delta^{18}\text{O}$ is $-23.3 \pm 0.15\text{‰}$ VPDB. The samples were cleaned in a methanol

281 ultrasonic bath for a few seconds and roasted under vacuum at 380 °C for 45 min prior to
282 analysis, in order to eliminate impurities (Duplessy, 1978). Oxygen-isotope data were recorded
283 from benthic foraminifera sampled in the GDEC-4, GDEC-6 and GDEC-8 cores (Figure 9): data
284 from the GDEC-4 core was especially important because it had the most complete sampling of
285 material for stable isotope analysis, and our seismic mapping indicated that it was in an area of
286 relatively continuous sedimentation. The $\delta^{18}\text{O}$ data provided age estimates for mapped seismic
287 surfaces by determining where these surfaces intersect the $\delta^{18}\text{O}$ curve in the GDEC-4 core, and
288 then matching the GDEC-4 $\delta^{18}\text{O}$ curves to the global stacked $\delta^{18}\text{O}$ curves of Lisiecki and Raymo
289 (2005). Oxygen isotope curves from GDEC-6 and GDEC-8 were not complete enough and too
290 disturbed by thick gravity flow deposits to be reliable for $\delta^{18}\text{O}$ analyses. A more detailed analysis
291 of isotope data from the GDEC- 4 core that emphasises climatic change is found in Toucanne et
292 al. (2015).

293

294 **MAPPING AND DATING SEISMIC HORIZONS**

295 Ten regional seismic horizons were dated. ^{14}C provided reliable ages back to ca. 48 ka,
296 OSL back to 127 ka, and matching $\delta^{18}\text{O}$ curves gave age control back to 478 ka (Figures 5, 9 and
297 10). The GDEC-4 core was particularly important for surfaces older than 91 ka because it has a
298 very complete $\delta^{18}\text{O}$ record that correlates well to the Lisiecki and Raymo (2005) global, stacked,
299 oxygen-isotope curves (Figure 9). In the GDEC-4 core, 9 thick marls were observed. These
300 marls could be correlated to marls in the other cores from the basin and were numbered 1
301 through 9 with 1 the youngest and 9 the oldest (Figure 5). They are interpreted to indicate
302 reduced clastic sedimentary input into the basin, similar to the carbonate-rich sediments that are
303 currently being deposited on abandoned parts of the South Golo Fan. These marls have depleted

304 $\delta^{18}\text{O}$ values that correlate to the episodes of depleted $\delta^{18}\text{O}$ in the global stacked $\delta^{18}\text{O}$ curves of
305 Lisiecki and Raymo (2005), hence penetration of these marls in the GDEC-4 core allows us to
306 provide age estimates for our deeper seismic horizons. These marl-rich horizons correspond to
307 very continuous, high-amplitude reflections with strong impedance contrasts, relative to the other
308 continuous seismic facies that have been tied to marl-free mudstones (Figure 6). The high
309 impedance contrast between marls and other sediments reflects their higher carbonate content,
310 lower porosity and higher density relative to the purely siliciclastic muds (e.g. Fig. 6).

311 There are limitations and uncertainties with our age model because GDEC-4 was the only
312 core that yielded a complete $\delta^{18}\text{O}$ curve. In most cases, specific $\delta^{18}\text{O}$ peaks did not directly
313 coincide with our seismic horizons, so we constrained seismic horizons by bracketing with older
314 and younger $\delta^{18}\text{O}$ markers. Moreover, the majority of our chronological constraints are
315 internally consistent with each other, and with the seismic data (Figure 10). There were some
316 divergences between dating techniques, for example, in the case of the 1100 FS and 1100 SB,
317 OSL ages from sands were younger than the age estimates obtained from $\delta^{18}\text{O}$ data from
318 overlying marls. OSL ages in this case may represent minimum ages for the deposition of the
319 host sediment that was sampled.

320 **SEDIMENT DISPERSAL THROUGH TIME**

321 While we mapped older sequences below core control this paper will only describe the
322 intervals for which we had core and seismic control. The oldest of these is bounded by the 700
323 and 800 sequence boundaries. The lowstand systems tract deposits are bounded the 700 SB and
324 the 700 FS (Figures 6 and 10). The 700 SB overlies a depletion spike on the $\delta^{18}\text{O}$ curves that we
325 associate with the MIS-12 sea-level lowstand at ca. 450 ka, when sea level was at -130 m relative
326 to present (Spratt and Lisiecki, 2016). We therefore interpret the downlapping seismic facies and

327 fan-shaped isopach map pattern of this interval within the deep basin to represent a sand-rich
328 submarine fan deposited during MIS 12. The isochron map of this interval suggests the presence
329 of one large fan fed by the merging of input from both the North and South Golo canyons
330 (Figure 11).

331 The transgressive and highstand systems tract deposits between the 700 FS and the 800
332 SB average ~8 m in thickness across the study area and are composed of high-amplitude,
333 continuous seismic facies that are mud-rich with locally high carbonate content in the GDEC-4
334 core (Figure 6). We interpret these deposits to represent the MIS 11 interglacial.

335 The next overlying sequence is bounded by the 800 SB and 900 SB. The lowstand
336 systems tract deposits between the 800 SB and 800 FS, are poorly constrained by $\delta^{18}\text{O}$ curves but
337 falls between horizons with age estimates of ca. 340 and 375 ka. The Waelbroeck et al. (2002)
338 sea-level curve places the MIS 10 glacial period of low sea level at -120 m relative to present,
339 between ca. 337 and 374 ka (Figure 10). We therefore interpret fan deposits above the 800 SB to
340 represent the MIS 10 glacial period, and the 800 FS to represent the beginning of the MIS 9
341 interglacial period. An isopach map of the lowstand systems tract deposits between the 800 SB
342 and the 800 FS shows two lobe-shaped sediment thicks, one associated with the North Golo
343 Canyon and one with the South Golo Canyon (Figure 11).

344 The GDEC-4 oxygen-isotope curve suggests that the fine-grained sediments between the
345 800 FS and the 900 SB, which include marl 8, were deposited during the MIS 9 interglacial
346 period of high sea level between 290 and 340 ka (Figure 6). The Waelbroeck et al. (2002) sea-
347 level curve shows an abrupt rise in sea level at ca. 340 ka, whereas our data suggest sand
348 delivery to the fan was terminated at this time, and a thick mud and marl-rich unit was deposited
349 until about 290 ka. The GDEC-4 oxygen-isotope curve suggests that fans deposited between the

350 900 SB and the 900 FS represent the MIS 8 glacial period of low sea level between ca. 240 and
351 290 ka (Figures 6 and 9). The GDEC-4 oxygen-isotope curve suggests that fine-grained
352 sediment in the interval between the 900 FS and the 1000 SB, including marls 4, 5, 6 and 7 were
353 deposited during the MIS 7 interglacial period of high sea level between ca. 190 and 240 ka
354 (Figures 6 and 9).

355 Isopachs of the overlying 1000 SB to 1000 FS interval show a thickness trend that
356 suggests deposition of one large fan was deflected to the south by the toe of slope of the Pianosa
357 Ridge (Figure 11). However, more detailed mapping and breaking out an internal surface shows
358 that there are two distinct fans, the oldest fed by the North Golo Canyon and the youngest fed by
359 the South Golo (Figure 11). OSL ages from sands in this interval in GDEC-8 are as old as ca.
360 127 ± 18.3 ka which are consistent with deposition near the end of the MIS 6 glacial period of
361 low sea level.

362 The interval between the top of the 1100 SB and the 1000 FS is penetrated by the GDEC-
363 4, GDEC-6 and GDEC-8 cores, is mud-rich, and is characterized by the occurrence of one or two
364 thick (> 1 m) marls (Figure 5). There are no OSL or ^{14}C dates from this unit, but the GDEC-4
365 oxygen-isotope curve suggests deposition between ca. 135 and 87 ka, corresponding to the MIS
366 5 interglacial period: global sea level was at or slightly higher than present day during MIS 5.5,
367 and oscillated between -20 and -60 m during MIS 5.3 to 5.1 (Siddall et al., 2003).

368 The interval between the 1100 SB and 1100 FS represents the period ca. 65.6 ka (based
369 on OSL ages) and ca. 15 ka (based on ^{14}C ages), which corresponds to MIS 4 and 2. This unit
370 can be divided between two distinct fans, which are separated by the 1300 SB. The older fan is
371 penetrated by the GDEC 8 core, yielded OSL ages of ca. 65.6 to 62.0 ka, and represents the MIS
372 4 glacial period of low sea level. The younger fan is penetrated by the GDEC 6 core, yielded

373 OSL ages and ^{14}C ages between ca. 31.7 ka and 16.7 ka, and represents the MIS 2 last glacial
374 maximum period of low sea level (Figure 5)

375 The 1100 FS is the shallowest zone that was mapped. OSL and ^{14}C dates show it to be
376 between 15 ka and 10 ka. A muddy or marly layer occurs throughout the basin at the seafloor,
377 although there appears to be some preserved Holocene sediment that was deposited ca. 400 to
378 800 years ago based on ^{14}C dates (Figure 5).

379

380 **DEPOSITIONAL ENVIRONMENTS**

381 The high-resolution bathymetric data acquired in this study provides a clear indication of
382 the depositional environments present today and in the recent past (Figure 2). When combined
383 with core and high-resolution seismic data, it was used to reconstruct how these environments
384 changed through time.

385

386 **Delta Lobes and Fluvial Channels on the Shelf**

387 The present-day Golo Delta is a wave-dominated delta with a pebbly to sandy topset and
388 shoreline, and distributary channels that are 30 to 75 m wide. High-resolution bathymetry and
389 seismic data show plan-view arcuate features with seaward-dipping internal reflectors at -50 m
390 and -80 m below current sea level (Figures 4 and 12). A similar prominent feature with seaward-
391 dipping reflectors is found at the modern shelf-slope break at -120 m below sea level (Figures 4
392 and 12). Cores from GDEC-1 and GDEC-3 demonstrate that sediment from the sea floor down to
393 50 mbsf through these features is composed of sand and gravel (Figure 5). As a result, we
394 interpret these them to be the seaward-dipping clinothems of older deltas abandoned on the now-
395 flooded shelf. Bathymetric and seismic data further reveal that these older deltas are arranged in

396 a back-stepping aggradational-retrogradational pattern, with the delta at -120 m being the oldest,
397 and the delta at -50 being the youngest (Figure 4). Using geochronological data, we interpret the
398 -120 clinothem to have formed ca. 20 ka and represent the MIS2 Last Glacial Maximum (LGM)
399 deltaic shoreline, the -80 m clinothem to have formed ca. 14 ka and represent progradation after
400 the onset of the Older Dryas cold period, and the -50 m clinothem to have formed ca. 12 ka with
401 progradation initiated during the Younger Dryas cold period and continuing into the Holocene
402 (Figure 12).

403 Seismic data from the shelf also reveal three types of east-west-trending elongate units in
404 the shallow part of the section, which cross-cut and truncate older strata and are filled with high-
405 amplitude discontinuous facies that are distinctive from the seaward-dipping deltaic clinothems
406 (Figure 4). An example of the first type is a 70 m-wide lenticular deposit just a few meters deep,
407 which is similar in size to the distributary channels of the modern Golo River, and interpreted to
408 represent a distributary channel of the Golo River when it was extended across the shelf to the -
409 50 m shoreline. The second type of elongate unit occurs buried at the head of both the North and
410 South Golo Canyons (Figure 13). These features can be mapped on multiple seismic lines, are up
411 to 2.5 km wide and 10's of meters in thickness, extend across the shelf from the western edge of
412 our seismic data (Figure 13), and are interpreted to represent cross-shelf paleovalleys (sensu
413 Blum et al., 2013) that were cut by the Golo River during periods of low sea level. The downdip
414 extension of the most recent paleovalley was penetrated by the GDEC 3 core between 10 and 18
415 mbsf, which sampled mostly fine to coarse sand and a small amount of conglomerate (Figures 4,
416 5 and 13a): ¹⁴C dates indicate this paleovalley was filled during the last 15 ka.

417 The third type of east-west trending erosional unit is also large but cuts deeper than
418 paleovalleys and pinches-out rapidly landward. Two examples are seen on seismic line Sigolo-

419 067 directly at the head of the South Golo Canyon (deepest features on Figure 13). The youngest
420 unit, which cuts into the previous one, reaches 70 m in depth and a kilometer in width. We
421 interpret these features as the updip extension of the South Golo Canyon as it underwent multiple
422 phases of cut and fill. Unfortunately, we have no core data to constrain the age or lithology of the
423 fill. However, the seismic horizon associated with one of these cuts (1100 SB) can be correlated
424 to the GDEC-1 core where OSL dating suggests that it is younger than 89 ka (Figure 5).

425 All of the above features, from the distributary channel-fill deposit to the paleovalley-
426 and canyon-fills suggest that the paleo-Golo River discharged directly into the heads of North
427 and South Golo canyons when sea level was low (Figure 14). In addition, Golo River sediment
428 appears to have been delivered to mouth bars that impinged on the head or margins of both
429 canyons until sea level was high enough to prevent the connection (Figures 10 and 14). This
430 relationship is especially clear for the -120 m deltaic clinothem, which represents the last glacial
431 maximum period of minimum sea level, whereas the regressive deltaic clinothem at -80 m,
432 which formed ca. 14 ka, is interpreted to be the last one to closely approach the head of the South
433 Golo Canyon (Figure, 4, 12, and 14). The 1100 SB represents the initiation of the connection
434 between a paleo-Golo River and the North and South Golo paleo-canyons and ends with a
435 disconnection that occurred sometime before deposition of the younger Dryas clinothem at ca. 12
436 ka. Disconnecting the Golo sand source from the canyon at ca. 14 ka is consistent with the
437 youngest sand seen in our data from the basin floor as well (Figure 5).

438

439 **Slope Canyons and Gullies**

440 The Golo margin in the study area is penetrated by two large submarine canyons (the
441 North and South Golo), two smaller canyons near the north edge of the study area (the Biguglia

442 and St. Domiano) and two straight, slope gullies, the Fium Alto and Pineto (Figure 12). The
443 North and South Golo canyons feed extensive submarine fans and appear to be the primary
444 conduits for sediment into the basin in our study area.

445 The South Golo Canyon reaches a maximum depth of 150 m. It penetrates about 1.5 km
446 headwards across the shelf from the shelf-slope break and extends 7 km down the slope. The
447 canyon begins to develop levees and makes the transition into a levee-confined channel at the
448 base of slope, in about 450 m water depth (Figures 12, 13, and 15). The canyon ranges in width
449 from 600 m at its head to a maximum of 3300 m. In the upper reaches, canyon edges are smooth
450 and the base of the canyon is flat. Seismic data indicate lateral migration of the South Golo
451 Canyon to the north through time. Further down the canyon prominent terraces develop (Figure
452 13). We have no core data from any of the canyons or gullies, but the moderate amplitude, high-
453 continuity seismic facies of the terraces suggest that they are composed of a heterolithic mix of
454 sand and mud. Similar lithologies have been reported by Jobe et al. (2015) from cores in
455 submarine canyons terraces off of the Niger Delta. The base of the canyon is filled with a low-
456 continuity, high- amplitude seismic facies that we interpret as coarse-grained sediments that
457 could be as coarse as the gravel-sized sediments seen in the GDEC-1 core from the Golo shelf.
458 The filling history of the canyon is complex with evidence of incision, lateral migration, and
459 aggradation of the fine-grained slope deposits outside of the canyon and coarse-grained deposits
460 in the deepest part of the canyon (Figure 13). Seismic data show that there are older, now
461 sediment-filled canyons below the most recent canyon. Cross-cutting relationships between the
462 canyon margins and dated seismic horizons suggest that the South Golo Canyon began to form at
463 least 450 ka ago, before the time of the 700 SB (Figure 13)

464 The North Golo Canyon and the nearby Pineto Gully were the sediment conduits for the
465 North Golo Fan (Figure 12). The North Golo Canyon penetrates headward about 1000 m into the
466 shelf. It ranges in width from 1100 to 1700 m and is up to 200 m deep. Seismic data show that at
467 least two older, sediment-filled canyons exist beneath the Pineto Gully which are on the scale of
468 the present-day North Golo Canyon.

469 In contrast to the North and South Golo canyons, which have sinuous planform
470 geometries, the smaller Pineto and Fium Alto gullies are narrow and straight (Figure 12). Cross-
471 cutting relationships observable in seismic data suggests they are young features formed by
472 collapse at the shelf-slope break without a long-lasting connection to a river-mouth or shoreline
473 feeder system on the shelf. The two gullies have preserved only a thin veneer of deposits since
474 they formed. The Fium Alto Gully ranges in width from 660 to 200 m and has a maximum depth
475 of 40 m. The lower reaches of the Fium Alto Gully, while largely erosional, also have low,
476 incipient levees. There is a small fan at the base of the slope at the terminal end of this gully that
477 is about 1.6 km wide and up to 24 m thick. The Pineto Gully ranges in width from 540 to 240 m
478 wide and up to 40 m deep. The lower reaches develop low levees and there is evidence from
479 seismic data of less erosion at the base of the gully and more aggradation of high-amplitude
480 discontinuous seismic facies that we interpret as coarse-grained deposits. One seismic line at the
481 terminus of the Pineto Gully shows a small (1.2 km wide), thin (about 20 m thick) fan that
482 developed downdip of the gully. Cross-cutting relationships with dated seismic horizons suggest
483 that the Pineto Gully has only existed since MIS-2.

484

485 **Levee-Confined Channels**

486 Both the North and South Golo fan channels are characterized by levee-confined reaches
487 (Figure 15). In the levee-confined reach of the South Golo, the channel is 400 to 600 m wide and
488 has levees that extend ~900-1500 m on either side of the channel to where they pinch out
489 forming wedge-shaped deposits. As observed by Skene et al. (2002) in their data of levee
490 heights, the Golo levees thicknesses decrease down channel toward the channel-lobe transition
491 (Figure 15). The South Golo channel extends 22 km from the South Golo Canyon to the channel-
492 lobe transition (Figure 15). The GDEC-8 core shows that the levee at that location is primarily
493 composed of mud with a few thin beds of fine to very fine sand and silt located near its base
494 (Figure 8). The composition of levee deposits in the more distal reaches of the South Golo
495 channel is not known.

496 The North Golo channel extends 10.3 km from the North Golo Canyon to the North Golo
497 Fan. A recent avulsion associated with the development of a large lobe complex at the toe of
498 slope explains the shorter length of the North Golo channel relative to its southern counterpart. In
499 a region down-dip of the latest lobe complex toward mid-basin, bathymetry indicates that the
500 North Golo channel extended farther out into the basin. In the levee-confined area, the North
501 Golo channel ranges from 800-1000 m wide and is situated between 50 m-high levees that
502 extend about a kilometer on either side of the channel. A 250 m-wide, slightly sinuous thalweg is
503 bordered by occasional terraces or internal levees, and represents the most recent path for
504 sediment-gravity flows before abandonment by avulsion.

505 **Lobes and Channel-Lobe Transitions**

506 As levees become lower and the relief of channels decreases basinward, large lobate
507 bodies develop, eventually occupying most of the lower-gradient regions. Their expression on
508 seismic data is characterized by a conformable, locally erosional base and a mounded top with
509 continuous to semi-continuous, high-amplitude reflections (Figure 16). Downlapping geometries
510 are observed along their basal margins (Figure 16). Following the nomenclature used by Pr elat et
511 al. (2010) we interpret these features as lobe complexes, as they represent the highest order of
512 lobate bodies that can be linked to an individual branch of a levee-confined channel. In this
513 model, avulsion along the levee-confined portion of the channel is necessary to initiate a new
514 lobe complex. Within lobe complexes, we then define a hierarchal set of nested components to
515 be lobes, lobe elements, bed sets and beds, with the basic principle that one or more components
516 stack to form the next larger component of the hierarchy (Pr elat et al., 2009).

517 On its most recent southerly path, the South Golo channel transitions into a lobe complex
518 12 km long and up to 10 km wide with a maximum thickness of 65 m. The GDEC-6 core
519 penetrates ~50 m of deposits dominated by fine sand (85%), but with grain sizes that range from
520 very fine sand to gravel (Figures 5 and 7). The mud in this core is typically expressed as meter-
521 thick beds that are interbedded with thicker beds of well-sorted sand (Figures 5, 7, and 16). The
522 lobe complex thins to 10-15 m towards its margins where it merges with a constant thickness
523 layer of low amplitude seismic facies that is very continuous throughout the basin. This unit,
524 where penetrated by cores GDEC-4 and GDEC-8 (Figures 6 and 8 respectively), is composed of
525 mud with silt laminations. The transition from the sandy lobe complex to the constant thickness
526 mud-rich unit can be gradational with high-amplitude reflectors from the lobe complex gradually

527 decreasing in amplitude, or it can be abrupt with sharp internal onlaps onto the lower amplitude
528 continuous reflectors of the regional unit (Figure 17).

529 Internal seismic geometries within the lobe complex show that it is composed of the
530 nested smaller bodies we interpret as lobes and lobe elements following the Prélat et al. (2010)
531 terminology (Figures 16 and 17). Within the lobe complex, individual lobes are bounded at the
532 base by bidirectional onlap and downlap, and at the GDEC-6 location they correspond to the
533 blocky sand packages with the thicker mud-rich units defining their upper and lower boundaries.
534 Six lobes have been identified within the South Golo lobe complex. They range in maximum
535 thickness between 20-30 m with dip-elongated shapes averaging 6 km long and 3 km wide. They
536 stack compensationally and show evidence of progradation, retrogradation, and lateral offset.
537 Individual lobes are connected to individual distributary channels that branch from the main
538 levee-confined channel upstream (Figure 16). None of these distributary channels or their lateral
539 deposits have been cored so the nature of their deposits are unknown, although the high
540 amplitude nature of their reflectors suggests a heterolithic composition overall.

541 Lobe elements are the smallest units that can be mapped with our seismic data, and
542 consist of packages of reflectors that thin toward the margins and thicken towards the center of
543 the lobe (Figure 16). We observe progressive upflow and lateral shifts in the locations of the
544 thickest part of these lobe elements. It is possible to distinguish 4 to 5 lobe elements within a
545 typical lobe, each with a maximum thickness of 5-15 m. Each lobe element has an elongated
546 shape with an average length of 8 km and an average width of 3 km. A central erosive feeder
547 channel is linked to unconfined deposits, a mouth bar, where the maximum thickness is
548 observed. When traversed by dip-oriented seismic lines, successive lobes elements appear as
549 shingled, retreating bodies with flat tops as opposed to “backsets” where the top of the sediment

550 body dips up-flow (Figure 16). Where penetrated in the GDEC-6 core, they are composed of
551 sand with grain size ranging from very fine to coarse sand, even at their margins (Figure 16). In
552 cross-section, lobe elements taper distally to a down-lap limit (present all along the mouth-bar
553 periphery) where they join a tabular section where the lobe-element fringe transitions from
554 interbedded mud and sand to bioturbated mud. The interpreted zero sand line occurs within the
555 lobe element fringe a few 100 m away from the down-lap limit. The retrogradational stacking of
556 lobe elements juxtaposes sand on sand between successive mouth-bars (Figure 16). The
557 retrograding mouth bars also end up overlaying preceding feeder channels building sandy
558 wedges that look like levees. At the scale of lobes, compensational stacking results in the inter-
559 fingering of sandy mouth-bars with muddy fringes from other lobes. The general distribution of
560 mud and sand in a lobe complex is illustrated in Figure 17.

561 The same geometries of lobes and lobe complexes can be observed within the lobe
562 complex attached to the North Golo channel as well as older lobe complexes throughout the
563 basin (Figure 16). The youngest lobe complex of the North Golo Fan developed at the location of
564 a recent avulsion from a well-developed levee-confined channel in the toe-of-slope area. Its base
565 is erosional at the location of the avulsion, becoming conformable downdip while its top is
566 mounded. At the avulsion location, the lobe complex develops on top of the abandoned channel-
567 levee system and it is difficult to distinguish the channel-fill deposits from the base of lobe
568 complex as the seismic facies are very similar (high amplitude, semi-continuous). Downdip of
569 the avulsion site the contact between the lobe and the abandoned levees is very sharp with clear
570 onlaps and downlaps of the lobe reflections onto the abandoned levee top (Figure 16). This lobe
571 complex reaches 6 km in length and 4 km in width and a maximum thickness of 30 m. It is built
572 with two or more lobes with clear internal backstepping geometries. A transition to regionally

573 continuous and parallel reflections occurs on the margins of the avulsion lobe complex in a
574 manner similar to the South Golo lobe complex. This layer thins to 7 m on the fringe of the lobe
575 complex (Figure 16b).

576 Well-developed lobe complexes are also expressed on the seafloor and on seismic lines at
577 the mouth of abandoned portions of the North and South Golo channels (Figure 17). They vary
578 in size, shape and thickness compared to the lobe complex attached to the latest South Golo
579 channel. These lobe complexes are between 5 and 10 km long, 4 and 8 km and 35 to 70 m thick.
580 The size and shape of the lobe complexes vary with the number of their constituent lobes and
581 their stacking patterns, which are all linked to avulsion processes. The governing factors for
582 location and frequency of avulsions will be discussed in a later section in parallel with the timing
583 of sedimentation in the basin and in relation to internal versus external forcings.

584 By contrast, lobe complexes attached to gullies are much smaller and are generally
585 composed of only one or two lobes. The Fium Alto Gully, in the southern part of the study area,
586 feeds a single lobe 5 km long and 3 km wide with a maximum thickness of 20 m. The Fium Alto
587 lobe was deposited at the toe-of-slope against the South Golo lobe, which prevented further
588 elongation. The Pineto Gully lobe, located between the North and South Golo canyons, reaches 8
589 km in length and 2 km in width. This is a very elongate lobe confined between the two leveed
590 channel systems. Over the Golo slope the gully lobes show larger ratios of lobe-element
591 thickness to channel depth than the lobe elements developed further downdip in the channel-
592 levee/lobe complexes. This characteristic has been linked by Hamilton et al. (2017) to the steeper
593 gradients on which they develop based on physical experiments validated by observations from
594 the Golo seismic data.

595

596 **DEPOSITIONAL RATES**

597 Depositional rates and sand-to-mud ratios for each of the sand-rich fans and the
598 associated mud-rich intervals we mapped are shown in Table 2. Sediment volumes have been
599 calculated inside an area of the basin where coverage by 2D seismic lines is sufficient to
600 accurately depict the boundaries between sand bodies. This area most likely does not cover the
601 entire reach of the fans and thus may underestimate the volume of sand and mud accumulated in
602 the basin as a whole. Age constraints for deposits less than ca. 100 ka in age are based on OSL
603 and ¹⁴C ages, and correlations between δ¹⁸O values in GDEC4 and global curves, whereas units
604 older than ca. 100 ka relied solely on δ¹⁸O data. Mud-rich intervals, which record deposition
605 during times of high relative sea level, are characterized by sedimentation rates of 0.07 to 0.17
606 m/ka, whereas periods of active sand-rich fan deposition occurred when sea level was low, and
607 had higher deposition rates of 0.35 to 0.59 m/ka. Deposition rates when sea level is low are
608 therefore 3-8 times greater than during periods of higher sea level, but the difference was not as
609 large as we had anticipated because muds dominate the overall sediment load, and significant
610 volumes of fine-grained sediment are dispersed across the basin, even in times of high sea level.
611 It is important to keep in mind that these rates are averaged over the entire basin and that
612 depositional rates at locations like an active channel-lobe transition must be much higher. The
613 most profound difference was the lack of sand deposited in the basin once sea level rose above -
614 80 m, relative to present, and Golo River sand supply became disconnected from the North and
615 South Golo canyons. Even during the Younger Dryas period of deltaic construction on the shelf,
616 the Golo River mouth did not come close enough to the canyon heads to allow sand to be
617 transferred to deep water.

618
619
620
621
622
623
624
625
626
627
628
629
630
631
632
633
634
635
636
637
638
639
640

DISCUSSION

Distribution of Sand Versus Mud Through Time

Consistent with existing sequence-stratigraphic models (e.g., Vail, 1987; Posamentier and Vail, 1988), deposition of sand in the Golo system reflects climate-forced sea-level controls, with sand-rich fans deposited when sea level was below about -80 m, the Golo River and delta had extended across the shelf, and there was a direct connection between the Golo River mouth and the upper reaches of submarine canyons and gullies. Deposition of significant volumes of mud and carbonate-rich sediments also occurred in the basin when sea level was rising and high, as previously shown at the GDEC-4 site (Toucanne et al., 2015). This observation is consistent with Sweet and Blum (2016) whose data showed that systems with narrow shelves should leak large quantities of mud into the basin even in times of relatively high sea level. It is likely that with better age control we would see rates of sedimentation decreasing over the last 14 ka when post-glacial sea-level rise was rapid (Deschamps et al., 2012), since the older (lower) part of the post-glacial succession is marked by mud deposition in the basin, and the youngest sediments at the seafloor are marls. Sømme et al. (2011) and Forzoni et al. (2015) argue that during periods of high sea level coarse-grained sediments are interred in onshore terraces and in the aggradational coastal plain. Our seismic data also suggest that coarse-grained sediments build delta lobes on the shelf when sea level is above -50 m, which are captured in the fill of cross-shelf paleovalley systems (Figures 12 and 13). Unfortunately, there are no published seismic data across the modern Golo Delta to determine the volume of sediment captured there. The modern delta is a very small feature and we imagine that the majority of coarse-grained sediments are captured in the alluvial plain during highstands. However, our cores and published data suggest

641 the Tyrrhenian Current sweeps the modern shelf of fine-grained sediment and transports it to the
642 north.

643 During glacial periods of low sea level, when the coastal plain part of the Golo River
644 incised through previous deposits and the channel extended across the shelf, sediment was
645 cannibalized from older fluvial terraces (Sømme et al., 2011; Forzoni et al., 2015) and shelf
646 deposits. Our mapping shows evidence of cross-shelf paleovalleys that connected the Golo River
647 directly to the North and South Golo canyons (Figure 13). During these periods mud was
648 partitioned in the basin into slope, mud-rich levees and the muddy fringes of the sand-rich fans.

649 The presence of multiple, stacked shelf edge deltas (Figure 4) demonstrates that
650 subsidence of the Golo shelf has created enough accommodation to preserve about 70 m of
651 coarse-grained sediment over the last 300 ka.

652

653 **Comparison to Other Quaternary Fans**

654 The North and South Golo fans have all of the depositional elements of other Quaternary
655 Fans like the Congo (Babonneau et al., 2002), Rhone (Droz and Bellaiche, 1985), Mississippi
656 (Weimer, 1989), Hueneme (Piper et al., 1999) and Danube (Popescu et al., 2001). They are fed
657 by submarine canyons, and turbidity currents then transit through a reach of levee-confined
658 channels to a down-dip, sand-rich fan. The sand-rich part of the fan has a lateral facies
659 relationship with a mud-rich fan fringe.

660 Smaller fans in tectonically active margins, like the Golo and Hueneme Fan of California
661 (Piper et al., 1999), display important differences from large passive-margins fans like the
662 Danube and Congo that go beyond the obvious differences in scale (10's versus 100's to 1000's of
663 km in extent and 10's versus 100's of m in thickness). Large passive-margin systems are

664 relatively unconfined on a low-gradient sea floor whereas the Golo is constrained by a sea floor
665 structural high (the Pianosa Ridge). The proportion of muddy leveed-channels versus sand-rich
666 fans vary greatly between fans like the Golo and their large passive-margin counterparts.
667 Moreover, fan lobes on the Golo display a back-stepping pattern of development that may be
668 characteristic of supercritical fans (Hamilton et al., 2017), and as a result the reach of levee-
669 confined channels is short relative to overall fan length. In the case of the active channel of the
670 Congo Fan the leveed channel extends for 1100 km feeding a terminal lobe that is about 35 km
671 long (Babonneau et al., 2002). Data on the recent channels of the Amazon Fan show similar
672 trends where the Brown Channel extends 580 km and feeds a lobe 45 km long (Jegou et al.,
673 2008). The resulting deposit of the entire fan consists largely of mud-rich levee deposits that are
674 interleaved with sand-rich terminal lobes. In the case of the Golo and other fans in tectonically
675 active margins, the levee-confined reaches are no more than 1.3 to 2.4 times the length of the
676 lobe. The overall result is a deposit that is more dominated by lobes than levees, though both are
677 present. Nonetheless the Golo differs from published models of sand-rich fans (e.g. Reading and
678 Richards, 1994) in that there are significant reaches of mud-rich, levee-confined channels that
679 separate the sand-rich lobes from the submarine canyon.

680 Our mapping and chronological framework shows that deep-water sediments of the
681 Corsica Basin can be divided into ~100 ka depositional sequences. The sequences can be divided
682 into shorter duration systems tracts. Lowstand systems tracts bounded at the base by regional
683 downlap (within sand-rich fan deposits), onlap and erosion, which we interpret to represent
684 classical sequence boundaries that record sea-level fall, extension of the Golo River across the
685 shelf, and initiation of sand delivery to the basin floor. The transgressive and highstand systems
686 tracts that compose the upper part of the sequence are composed of up to 10 m thick packages of

687 mud and marl, which are interpreted to represent sea-level rise and flooding of the shelf,
688 backstepping of the Golo River mouth, and cessation of sand delivery to the basin. Our youngest
689 depositional sequence represents the last 100 ka glacial-interglacial cycle (MIS 5-1), but can be
690 further subdivided due to higher-resolution chronological control: for this sequence we
691 differentiate distinct cross-shelf extension of the Golo River to the shelf margin, and sand-rich
692 fan deposition on the basin floor, during the MIS 4 and 2 periods of low sea level, with
693 backstepping of the Golo River and cessation of sand delivery during the intervening MIS 3
694 period of sea-level rise to mid shelf positions. Sweet and Blum (2016) suggest this higher-
695 frequency change should be characteristic of small systems with inherently narrow shelves,
696 which would contrast with large systems with wide shelves, where sand-rich deposition may be
697 restricted to the MIS 2 last-glacial maximum sea-level lowstand.

698 Last, within and between individual depositional sequences we observed shifts of
699 depocenters where sand was routed down either the North or South Golo Canyon, and coeval
700 muddy deposits blanketed the rest of the basin. We interpret these changes to have been driven
701 by autogenic avulsion processes acting in the lower reaches of the Golo River, and/or on the
702 Golo Delta, which caused the Golo River to connect with, and the sand load to be routed down,
703 by turns, the North or South Golo canyons. Although of a different scale, Blum et al. (2018)
704 interpreted similar signals of autogenic avulsion of the Ganges-Brahmaputra Rivers within the
705 deep-sea Bengal Fan.

706

707 **CONCLUSIONS**

708 1) Connections for sand movement between fluvial/deltaic systems and submarine canyons
709 occur when shorelines migrate basinward, paleo-valleys cut the shelf during periods of

710 sea-level fall, and river mouths or deltaic lobes connect directly with the heads of
711 submarine canyons. Even given the relatively narrow shelf of the eastern Corsica margin,
712 sand transport to the fans is restricted to relatively small percentages of time when sea
713 level was -80 m or more below its current level and the Golo River and/or delta had a
714 direct connection to the heads of the North or South Golo Canyon. In contrast, mud can
715 be advected up to several kilometers across the shelf and, as a result, mud deposition
716 occurs over a much wider range of sea level conditions and represents a significantly
717 larger percentage of time.

718 2) Canyon evolution on the Golo shelf margin and slope includes some incision, but also
719 aggradation of entire margin and of canyon-fill deposits. Canyons migrated laterally and
720 are from time to time abandoned and filled. The main feeder canyons of the Golo system
721 are long-lived having begun form at least 450 ka ago.

722 3) The reach of levee-confined channels is short compared to large passive-margin systems
723 like the Danube, Amazon and Congo. Levee to lobe length is in the ratio of 1:1 or 1.5:1
724 on the Golo compared to 10's:1 in the case of the Congo, Danube and Amazon. This is
725 significant because large quantities of mud are trapped in the levees of large fans, whereas
726 mud in the Golo system occurs as drapes and as extensive muddy fringes to the sandy
727 lobes. This is distribution of mud is probably characteristic of most short, steep fans like
728 the Golo.

729 4) Deposition rates in the deep basin vary by a factor of up eight times between periods of
730 low versus rising or high sea level. Sand deposition appears to be restricted to periods of
731 low sea level (-80 m below present), when river mouths are proximal (within ~2 km) to
732 canyon heads.

733 5) Response of the Golo River to allogenic, climate-forced sea-level change plays the
734 overarching role in determining rates and grain size of sediment supplied to the basin.
735 However, autogenic factors such as avulsion of the Golo River and its deltaic system
736 laterally across the shelf, and avulsion and lobe switching on the submarine fans
737 themselves, control where deposition of sand-sized sediment is localized within
738 depositional sequences.

739 **ACKNOWLEDGEMENTS**

740 The late Bruno Savoye first proposed the idea of a detailed seismic and coring program
741 on the Golo system. He was instrumental in acquiring the 2D seismic data, but tragically died
742 soon afterward. This study would have been impossible without his work. Gilles Lericolais
743 played an important role in coordinating the study from Ifremer after Bruno's death, and in
744 planning the coring program. Funding came from a consortium of the Institut français de
745 recherche pour l'exploitation de la mer (Ifremer), Total E&P Recherche Developpment,
746 ExxonMobil Upstream Research Company, and Fugro N.V. We acknowledge ExxonMobil
747 Research Company for supporting our work and giving us permission to publish. The captain
748 and crew of the RV *Le Suroit* showed great skill in acquiring the 2D seismic survey and high-
749 resolution bathymetry used in this study. The captain and crew of the drillship *Bavenit* did an
750 outstanding job of cutting core in a very challenging mix of lithologies. Over the years a number
751 of geoscientists at ExxonMobil, Ifremer, and Total have contributed to the Golo project. We
752 acknowledge Vitor Abreu, Martine Bez, Gérome Calves, Simon Charrier, Bernard Dennielou,
753 Tina Drexler, Laurence Droz, Francis Ezeh, Gilbert Floch, Isabelle Jégou, Stephan Jorry, Katie
754 Love, Bill Heins, Caroline Labaune, Elodie Marches, Angélique Roubi, and Mickael Rovere for
755 their contributions to this project. Our ExxonMobil colleagues Paul Dunn, Howard Feldman,

756 David Hoyal, and Mauricio Perillo read drafts of this paper and challenged us to clarify our ideas
757 and our writing. GSA Bulletin Science Editor Dr. Rob Strachan, Associate Editor Dr. Rajat
758 Mazumder, and reviewer Dr. Octavian Catuneanu provided important suggestions to help us
759 improve the final quality of our paper. We extend a special thanks to GSA reviewer Dr. Richard
760 N. Hiscott who very carefully reviewed the manuscript twice and caught many errors and
761 inconstancies in the text.
762

763 **REFERENCES**

- 764 Aitken, M.J., 1998, An introduction to optical dating: The dating of Quaternary sediments by the
765 use of photon-stimulated luminescence: Oxford, University Press, 267 p.
- 766 Astraldi, M. and Gasparini, G.P., 1992, The seasonal characteristics of the circulation in the
767 north Mediterranean Basin and their relationship with the atmospheric-climatic
768 conditions: *Journal of Geophysical Research*, v. 97, p. 9531 – 9540.
- 769 Babonneau, N., Savoye, B., Cremer, M., and Klein, B., 2002, Morphology and architecture of
770 the present canyon and channel system of the Zaire deep-sea fan: *Marine and Petroleum*
771 *Geology*, v. 19, p. 445 - 467.
- 772 Bellaiche, G., Droz, L., Gaullier, V., and Pautot, G., 1994, Small submarine fans on the eastern
773 margin of Corsica: sedimentary significance and tectonic implications: *Marine Geology*,
774 v. 117, p. 177 – 185.
- 775 Blum, M. D., Martin, J., Milliken, K., and Garvin, M., 2013, Paleovalley systems: Insights from
776 Quaternary analogs and experiments: *Earth-Science Reviews*, v. 116, p. 128 – 169.

777 Blum, M. D., Rogers, K. G., Gleason, J. D., and Najman, Y., 2018, Fingerprints of Climate
778 Change in the Detrital-Zircon U-Pb Record of the Deep-Sea Bengal Fan? : American
779 Geophysical Union, Fall Meeting 2018, abstract #T23C-0386.

780 Calves, G., Toucanne, S., Jouet, G., Charrier, S., Thereau, E., Etoubleau, J., Marsset, T.,
781 Droz, L., Bez, M., Abreu, V., Jory, S., Mulder T., and Lericolais, G., 2013, Inferring
782 the denudation variations from the sediment record; an example of the last glacial cycle
783 record of the Golo Basin and watershed, East Corsica, western Mediterranean Sea: Basin
784 Research, v. 25, p. 197 - 218.

785 Catuneanu, O., 2019, Model-independent sequence stratigraphy. *Earth-Science Reviews*, v. 188,
786 p. 312-388.

787 Deptuck, M. E., Piper, D. J. W., Savoye, B., Gervais, A., 2008, Dimensions and architecture of
788 late Pleistocene submarine lobes off the northern margin of East Corsica: *Sedimentology*,
789 v. 55, p. 869 - 898.

790 Deschamps, P., Durand, N., Bard, E., Hamelin, B., Camion, Thomas, A. L., Henderson, G. M.,
791 Okuno, J., and Yokoyama, Y., 2012, Ice-sheet collapse and sea-level rise at the Bolling
792 warming 14,600 years ago: *Nature*, v. 483, p. 559 – 564, doi: 10.1038/nature10902 .

793 Droz, L., and Bellaiche, G., 1985, Rhone deep-sea fan: Morphostructure and growth patterns:
794 *American Association of Petroleum Geologists, Bulletin*, v. 69, p. 460 – 479.

795 Duplessy, J.C., 1978, *Isotope studies: Climatic change*, v. 3, p. 47-67.

796 Forzoni, A., Storms, J. E. A., Reimann, T., Moreau, J. and Jouet, G., 2015, Non-linear response
797 of the Golo River system, Corsica, France to Late Quaternary climatic and sea level
798 variations: *Quaternary Science Reviews*, v. 121, p. 11 – 27.

799 Gervais, A., 2002, Analyse multi-échelle de la morphologie, de la géométrie et de l'architecture
800 d'un système turbiditique sableux profond (System du Golo Marge est-Corse, Mer
801 Méditerranée). Ph.D. Dissertation University of Bordeaux, 285 p.

802 Gervais, A., Savoye, B., Piper, D. J. W., Mulder, T., Cremer, M., and Pichevin, L., 2004, Present
803 morphology and depositional architecture of a sandy confined submarine system: the
804 Golo turbidite system (eastern margin of Corsica), *in* Lomas, S. A. and Joseph, P., eds.,
805 Confined Turbidite Systems: London, Geological Society [London] Special Publication,
806 v. 22, p. 59 – 89.

807 Gervais, A., Mulder, T., Savoye, B., and Gonthier, E., 2006, Sediment distribution and evolution
808 of sedimentary processes in a small sandy turbidite system (Golo system, Mediterranean
809 Sea): implications for various geometries based on core: *Geo-Marine Letters*, v. 26, p.
810 373-395.

811 Gabin, R., 1972, Resultats d'un etude sismique reflexion dans le canal do Corse, et de sondeur de
812 vase dans le bassin Toscan : *Marine Geology*, v. 13, p. 267 – 286.

813 Hamilton, P., Gaillot, G., Strom, K., Fedele, J., Hoyal, D., 2017, Linking hydraulic properties in
814 supercritical submarine distributary channels to depositional-lobe geometry: *Journal of*
815 *Sedimentary Research*, v. 87, p. 935-950.

816 Hsu, K., 1973, The desiccated deep-basin for the Messinian events: *In* Drooger, C. W., ed., *The*
817 *Messinian Events in the Mediterranean*: Amsterdam, North Holland Publishing Co., p.
818 60-67.

819 Jegou., I., Savoye, B., Pirmez, C., and Droz, L., 2008, Channel-mouth lobe complex of the recent
820 Amazon Fan: the missing piece: *Marine Geology*, v. 252, p. 62 -77.

821 Jobe, Z.R., Sylvester, Z., Parker, A.O., Howes, N., Slowey, N., and Pirmez, C., 2015, Rapid
822 adjustment of submarine channel architecture to changes in sediment supply: *Journal of*
823 *Sedimentary Research*, v. 85, p. 729–753, doi: 10.2110/jsr.2015.30.

824 Jolivet, L., Faccenna, C., Goffé, B., Mattei, M., Rossetti, F., Brunet, C., Storti, F., Funicello, R.,
825 Cadet, J. P., d’Agostino, N., and Parra, T., 1998, Midcrustal shear zones in postorogenic
826 extension: Example from the Tyrrhenian Sea: *Journal of Geophysical Research*, v. 103, p.
827 12,123 – 12,160.

828 Jouet, G., 2018, GOLODRILL cruise, RV Bavenit, <https://doi.org/10.17600/18000744>

829 Lisiecki, L. E. and Raymo, L. E., 2005, A Plio-Pleistocene stack of 57 globally distributed
830 benthic δ^{18} records: *Paleoceanography*, v. 20, PA1003.

831 Mauffert, A., Contrucci, I., and Brunet, C., 1999, Structural evolution of the Northern Tyrrhenian
832 Sea from new seismic data: *Marine and Petroleum Geology*, v. 16, p. 381 – 407.

833 Maier, K. L., Fildani, A., McHargue, T. R., Paull, C. K., Graham, S. A., and Caress, D.W., 2012,
834 Punctuated deep-water channel migration: high-resolution subsurface data from the Lucia
835 Chica Channel system, offshore California, USA: *Journal of Sedimentary Research*, v.
836 82, p. 1 – 8.

837 Minto’o, C. M. A, Bassetti, M-A., Toucanne, S., and Jouet, G., 2016, Distribution of ostracod
838 and benthic foraminiferal assemblages during the last 550 kyr in the East-Corsica basin,
839 western Mediterranean Sea: a paleo-environmental reconstruction: *Revue de*
840 *Micropaléontologie*, v. 59, p. 83 – 96.

841 Miramontes, E., Cattaneo, A., Jouet, G., and Garzigalia, S., 2016a, Implications of sediment
842 dynamics in mass transport along the Pianosa Ridge (Northern Tyrrhenian Sea): *in* G.
843 Lamarche, ed. *Submarine Mass Movements and their Consequences*, *Advances in*

844 Natural and Technological Hazards Research 41, Springer International Publishing
845 Switzerland, p. 301-309.

846 Miramontes, E., Cattaneo, A., Jouet, G., Thereau, E., Thomas, Y., Rovere, M., Cauquil, E.,
847 Trincardi, F., 2016b, The Pianosa contourite depositional system (Northern Tyrrhenian
848 Sea): drift morphology and Plio-Quaternary stratigraphy: *Marine Geology*, v. 378, p. 20 –
849 42.

850 Mitchum, R. M., 1985, Seismic stratigraphic expression of submarine fan, *in*, O. R. Berg and D.
851 G. Woolverton, eds., *Seismic Stratigraphy II: An integrated approach to hydrocarbon*
852 *exploration: Tulsa, AAPG Memoir 39*, p. 117 -136.

853 Mulder, T. and Maneaux, E., 1999, Flux et bilan sédimentaires. Impact d'apports fluviale sur la
854 construction des éventails sous-marin profond de la marge Est-Corse, Université
855 Bordeaux I, Rapport interne, p. 20.

856 Murray, A. S. and Wintle, A. G., 2000, Luminescence dating of quartz using an improved
857 single-aliquot regenerative-dose protocol: *Radiation Measurements*, v. 32, p. 57-73.

858 Murray, A. S. and Wintle, A. G., 2003, The single aliquot regenerative dose protocol: potential
859 for improvements in reliability: *Radiation Measurements*, v. 37, p. 377-381.

860 Neal, J and Abreu, V., 2009, Sequence stratigraphy hierarchy and the accommodation succession
861 method: *Geology*, v. 37, p. 779 – 782.

862 Paull, C.K., Caress, D.W., Lundsten, E., Gwiazda, R., Anderson, K., McGann, M., Conrad, J.,
863 Edwards, B., and Summer, E.J., 2013, Anatomy of La Jolla Canyon system; offshore
864 southern California: *Marine Geology*, v. 335, p. 16 -34.

865 Picot, M., Droz, L., Marsset, T., Dennielou, B., Bez, M., 2016, Controls on turbidite
866 sedimentation: Insights from a quantitative approach of submarine channel and lobe

867 architecture (Late Quaternary Congo Fan): *Marine and Petroleum Geology*, v. 72, p. 423-
868 446.

869 Piper, D.J.W., Hiscott, R. N., and Normark, R. W., 1999, Outcrop-scale acoustic facies and latest
870 Quaternary development of Hueneme and Dume submarine fans, offshore California:
871 *Sedimentology*, v. 46, p. 47 – 78.

872 Pluquet, F., 2006. Evolution récente et sédimentation des plates-formes continentales de la
873 Corse. Doctorat, Université de Corse, France.

874 Popescu, I., Lericolais, G., Panin, N., Wong, H.K., and Droz, L., 2001, Late Quaternary
875 avulsions on the Danube deep-sea fan, Black Sea: *Marine Geology*, v. 179, p. 25 -37.

876 Posamentier, H. W, and Vail, P. R., 1988, Eustatic controls on clastic deposition II – Sequence
877 and Systems Tract Models, *in*, Wilgus, C. K., Hastings, B. S., Posamentier, H., Van
878 Wagoner, J., Ross, C.A. and Kendall, C. G. St. C., eds., *Sea Level Changes – An*
879 *Integrated Approach*: Tulsa, SEPM Special Publication 42, p. 125 – 154.

880 Prélat, A., Covault, J.A., Hodgson, D.M., Fildani, A., and Flint, S.S. 2010, Intrinsic controls on
881 the range of volumes, morphologies, and dimensions of submarine lobes: *Sedimentary*
882 *Geology*, v. 232, p. 66–76.

883 Prélat, A., Hodgson, D.M., Flint, S.S., 2009. Evolution, architecture and hierarchy of distributary
884 deep-water deposits: a high-resolution outcrop investigation the Permian Karoo Basin,
885 South Africa: *Sedimentology* v. 56, p. 2132–2154.

886 Reading, H.G. and Richards, M., 1994, Turbidite systems in deep-water basin margins classified
887 by grain size and feeder system: *American Association of Petroleum Geologists Bulletin*
888 v. 78, p. 792 – 822.

889 Reimer, P. J., Baillie, M. G. L., Bard, E., and Bayliss, A., 2009, Intcal09 and marine 09
890 radiocarbon age calibration curves, 0-50,000 years cal BP: Radiocarbon, v. 51, p.1111-
891 1150.

892 Rittenour, T. M., Goble, R. J. and Blum, M. D., 2003, An Optical Age Chronology of Fluvial
893 Deposits in the Northern Lower Mississippi Valley: Quaternary Science Reviews, v. 22,
894 p. 1105-1110.

895 Rittenour, T. M., Goble, R. J., and Blum, M. D., 2005, Development of an OSL chronology for
896 late Pleistocene channel belts in the lower Mississippi valley: Quaternary Science
897 Reviews, v. 24, p. 2539-2554.

898 Ryan, W. B., 2009, Decoding the Mediterranean salinity crisis: Sedimentology, v. 56, p. 95 –
899 136.

900 Savoye B., 2008, SIGOLO cruise, RV Le Suroît, <https://doi.org/10.17600/8020110>.

901 Shackelton, N.J., 2000, The 100,000-Year Ice-Age Cycle Identified and Found to Lag
902 Temperature, Carbon Dioxide, and Orbital Eccentricity : Science, v. 289, p. 1897 – 1902.

903 Siani, G., Paterne, M., Michel, E., Sulpizio, R., Sbrana, A., Arnold, M., Haddad, G., 2001,
904 Mediterranean Sea surface radiocarbon reservoir age changes since the last glacial
905 maximum: Science, v. 294, p. 1917-1920.

906 Siddall, M., Rohling, E.J., Almogi-Labin, A., Hemleben, Ch., Meischner, D., Schmelzer, I., and
907 Smeed, D.A., 2003, Sea-level fluctuations during the last glacial cycle: Nature, v. 423, p.
908 853 – 858.

909 Skene, K. I., Piper, D. J. W., and Hill, P. S., 2002, Quantitative analysis of variations in
910 depositional sequence thickness from submarine channel levees: Sedimentology, v. 49, p.
911 1411 – 1430.

912 Sømme T. O., D. J. W. Piper, M. E. Deptuk and W. Helland-Hansen, 2011, Linking onshore-
913 offshore sediment dispersal in the Golo source-to-sink system (Corsica, France) during
914 the late Quaternary: *Journal of Sedimentary Research*, v. 81, p. 118 – 137.

915 Spratt, R. M. and Lisiecki, L. E., 2016, A Late Pleistocene sea level stack: *Climate Past*, v. 12, p.
916 1079-1092, <https://doi.org/10.5194/cp-12-1079-2016>, 2016

917 Stanley, D. J., Rehault, J. P., and Stuckenrath, R., 1980, Turbid-layer bypassing model: The
918 Corsica Trough, northwestern Mediterranean: *Marine Geology*, v. 37, p. 19 – 40.

919 Stuiver, M., and Reimer, P., 1993, Extended ¹⁴C Data Base and Revised CALIB 3.0 ¹⁴C Age
920 Calibration Program: *Radiocarbon*, v. 35, p. 215-230. doi:10.1017/S0033822200013904

921 Sweet, M. L. and Blum M. D., 2016, Connections between fluvial to shallow marine
922 environments and submarine canyons: Implications for sediment transfer to deep water:
923 *Journal of Sedimentary Research*, v. 86, p. 1147 – 1162.

924 Sylvester, Z., Deptuk, M.E., Prather, B.E., Pirmez, C., and O’Byrne, C., 2012, Seismic
925 stratigraphy of a shelf-edge delta and linked submarine channels in the northeastern Gulf
926 of Mexico, *in* Prather, B.E., Deptuk, M.E., Mohrig, D., Van Hoorn, B., and Wynn, R. B.,
927 eds, *Application of the Principles of Seismic Geomorphology to Continental-Slope and*
928 *Base-of-Slope Systems: Case Studies from Seafloor and Near-Seafloor Analogues*: Tulsa,
929 SEPM, Special Publication 99, p. 31 – 59.

930 Toucanne, S., Angue Minto'o, C.M., Fontanier, C., Bassetti, M.-A., Jorry, S.J., Jouet, G., 2015,
931 Tracking rainfall in the northern Mediterranean borderlands during sapropel deposition,
932 *Quaternary Science Reviews*, v. 129, p. 178-195.

- 933 Vail, P. R. 1987, Part 1: Seismic stratigraphy interpretation procedure, *in* Bally, A. W., ed., Atlas
934 of Seismic Stratigraphy, Volume 1: Tulsa, American Association of Petroleum
935 Geologists Studies in Geology 27, p. 1 – 10.
- 936 Van Wagoner, J.C., Mitchum Jr., R.M., Campion, K.M., Rahmanian, V.D., 1990, Siliciclastic
937 sequence stratigraphy in well logs, core, and outcrops: concepts for high resolution
938 correlation of time and facies, Methods in Exploration Series, v. 7: Tulsa, American
939 Association of Petroleum Geologists, 55 p.
- 940 Weimer, P., 1989, Sequence stratigraphy of the Mississippi Fan (Plio-Pleistocene), Gulf of
941 Mexico: GeoMarine Letters, v. 9, p. 185 – 272.
- 942 Waelbroeck C., Labeyrie, L., Michel, E., Duplessy, J. C., McManus, J. F., Lambeck, K., Balbon,
943 E., and Labracherie, M.,2002, Sea-level and deep water temperature changes derived
944 from benthic foraminifera isotopic records: Quaternary Science Reviews, v. 21, p. 295 –
945 305.
- 946 Wintle, A. G. and A. S., Murray, 2006, A review of quartz optically stimulated luminescence
947 characteristics and their relevance in single-aliquot regenerative protocols: Radiation
948 Measurements, v. 41, p. 369-391.
949

950 **FIGURE CAPTIONS**

951 Figure 1. Elevation map of Corsica (ASTER V2 GDEM 30m resolution) and bathymetry of the
952 Corsica Basin (TCarta's bathymetric grid derived from 1:2000, 000 scale charts and 1:60,000
953 scale coastline from Landsat imagery at 90 m seafloor resolution) showing the study area (white
954 box), location of the modern Golo fans and the Golo River drainage basin. Contours of
955 submarine channels and lobes modified from Figure IV-28 in Gervais (2002). Imagery licensed
956 by agreement with Spatial Energy (slb@SpatialEnergy.com).

957 Figure 2. Map of multi-beam bathymetry from the 2008 SIGOLO survey, 10 m resolution; 25 m
958 grid spacing. Water depth in meters. In addition to bathymetry this map shows the location of the
959 seismic lines (in white) acquired in the 2008 SIGOLO survey and the GDEC cores cut in 2009
960 coring campaign. SGC – South Golo Canyon. NGC – North Golo Canyon. Contour Interval = 10
961 m. The location of seismic lines used in the figures are numbered by figure and shown with
962 heavier dark lines.

963 Figure 3. Seismic line Sigolo-081 showing geometries and facies used to construct the seismic
964 stratigraphic framework. Seismic facies are High Amplitude Semi-Continuous (HASC) and High
965 Amplitude Continuous (HAC). Core data indicate that HASC facies are sand-rich, while HAC
966 are mud-rich with interbedded marls. Sequence boundaries (SB) are shown as solid lines. They
967 are characterized by incision/truncation and downlap/onlap (arrows). Flooding surfaces (FS) are
968 shown as dashed lines. They are characterized by draping geometries and very high continuity of
969 seismic events. V.E. = X15.

970 Figure 4. Seismic line Sigolo-034b showing the geometry of the Golo shelf, slope and underlying
971 deposits. Grain size of the GDEC-1 and GDEC-3 cores (green = silt and clay, yellow = sand,
972 orange = gravel) and their tie to seismic data are also shown. V.E. = X8.

973 Figure 5. Cross-section showing the 5 cores cut for this study, their lithologies, ages and
974 stratigraphic relations. Core depths are in meters below seafloor. Age data in years from ^{14}C
975 (black), OSL (red) and $\delta^{18}\text{O}$ (green) are shown. Marls shown in blue, sequence boundaries in red
976 and flooding surfaces in green are correlated using seismic and age data.

977 Figure 6. Seismic line Sigolo-085 across the Corsica slope crossing the location of the GDEC-4
978 core with median grain size (D50) and calcimetry logs shown to calibrate seismic facies.
979 Lowstand systems tract deposits (e.g. G1100 etc.) are shown bounded at the base by sequence
980 boundaries in red (e.g. 1100 SB etc.) and top by flooding surfaces in green (e.g. 1100 FS etc.).
981 V.E. = X7.

982 Figure 7. Seismic line Sigolo-058 on the South Golo Fan showing the location of the GDEC-6
983 core with median grain size (D50) and calcimetry logs shown to calibrate seismic facies.
984 Location of marly intervals interpreted on cores are highlighted in blue. Lowstand systems tract
985 deposits (e.g. G1100 etc.) are shown bounded at the base by sequence boundaries in red (e.g.
986 1100 SB etc.) and top by flooding surfaces in green (e.g. 1100 FS etc.). The 1300 SB is an
987 internal surface within the 1100 sequence that records base of an MIS-4 fan. V.E. = X7.

988 Figure 8. Seismic line Sigolo-007 on the South Golo Channel showing the location of the
989 GDEC-8 core with median grain size (D50) and calcimetry logs shown to calibrate seismic
990 facies. Lowstand systems tract deposits (e.g. G1100 etc.) are shown bounded at the base by
991 sequence boundaries in red (e.g. 1100 SB etc.) and top by flooding surfaces in green (e.g. 1100
992 FS etc.). V.E. = X7.

993 Figure 9. Oxygen isotope curves from benthic foraminifera sampled in the GDEC-4, 6, and 8
994 cores compared to the global standard of Lisiecki and Raymo (2005). Ages are labelled on the

995 vertical axis of the Lisiecki and Raymo (2005) curve while the curves from the GDEC cores are
996 plotted in depth (mbsf) with interpreted oxygen isotope stages shown.

997 Figure 10. Age model for the Corsica Trough. The upper panel shows the depths of age
998 measurements from OSL and ^{14}C and age estimates from $\delta^{18}\text{O}$ curves from the GDEC 4, 6, and 8
999 cores. Age estimates for lowstand systems tract deposits are shown in the colored boxes. The
1000 lower panel shows composite mean sea level curve (thick gray line) after Waelbroeck et al.
1001 (2002) plotted along with Shackleton's (2000) mean water $\delta^{18}\text{O}$ curve (dotted blue line). Marine
1002 Oxygen Isotope Stages are also shown on the sea level (bold, black numbers). Lowstand systems
1003 tract deposits are shown in colors, highstand systems tract deposits are in white.

1004 Figure 11. Isopach maps of 5 lowstand systems tracts interpreted in this study. Note that
1005 individual submarine fans are associated with either the north or south Golo Canyons. Dashed
1006 red lines show the interpreted direction of sediment transport.

1007 Figure 12. Shaded bathymetry of the Corsica shelf, slope, and trough showing the location of the
1008 North (NGC) and South Golo canyons (SGC), South Golo Fan (SGF), Fuim Alto Gulley (FG),
1009 Pineto Gulley (PG), cores used in this study (GDEC-1 etc.), the LGM shoreline at -120 m and
1010 lobe-shaped bathymetric features interpreted as relict deltaic lobes. Seismic line A-A' illustrates
1011 a deltaic lobe with clinoforms (DC) that impinged on the edge of the South Golo Canyon when
1012 sea level was about -80 m below current sea level and the delta fed sediment directly into the
1013 canyon.

1014 Figure 13. Bathymetric map showing the location of two seismic lines (A – A' and B – B'), the
1015 updip extent of the South Golo Canyon beneath the modern shelf (solid black lines) and the
1016 extent of the larger MIS-2 paleo-valley (thick, gray cross-hatched lines on the shelf). A) Seismic
1017 line Sigolo-067 illustrates the updip extent of the South Golo Canyon where it has merged with

1018 the MIS-4 (1100 SB) paleo-valley of the Golo River. B) Seismic line Sigolo-021 in the lower
1019 reaches of the South Golo Canyon illustrates the cross-sectional shape of the canyon and the
1020 aggradational nature of deposits adjacent to the canyon. High amplitude discontinuous seismic
1021 facies (HDC) interpreted as a coarse sand and gravel are restricted to the deepest part of the
1022 canyon and also show aggradational stacking.

1023

1024 Figure 14. Shaded bathymetry of the Corsica shelf and slope showing location of the shoreline
1025 from 1100 SB (MIS-4) to the 1600 surface (Younger Dryas) in relation to the North and South
1026 Golo canyons.

1027 Figure 15. Seismic lines: A) Sigolo-086; B) Sigolo-07; and C) Sigolo-51 showing down-channel
1028 changes in levee height and geometry along the South Golo channel. V.E. = X 5. Location map
1029 shows bathymetry in meters (C.I. = 25 m) and the location of the seismic lines.

1030 Figure 16. Bathymetric map showing the distribution of lobate bodies attached to channel-levee
1031 systems and gullies throughout the basin that were deposited during MIS-2 and MIS-4. Seismic
1032 lines A and B show lobe geometries associated with a fan fed by the North Golo Canyon.
1033 Seismic lines C (Sigolo-058) and D (Sigolo-004) show strike (C) and dip (D) profiles across the
1034 most recent South Golo lobe complex revealing the internal geometries of small-scale lobes and
1035 lobe elements. HAD – High-Amplitude Discontinuous seismic facies, HAC - High-Amplitude
1036 Continuous seismic facies, LAC – Low-Amplitude Continuous seismic facies. V. E. = X 15.

1037 Figure 17. Schematic representation of the hierarchy of channel-form and distributive lobe
1038 bodies observed in the South Golo Canyon (Fairway) and at the mouth of its channel. The grain
1039 size log from core GEC-6 gives a vertical representation of the lithology of the lobe hierarchy.

1040 **TABLE CAPTIONS**

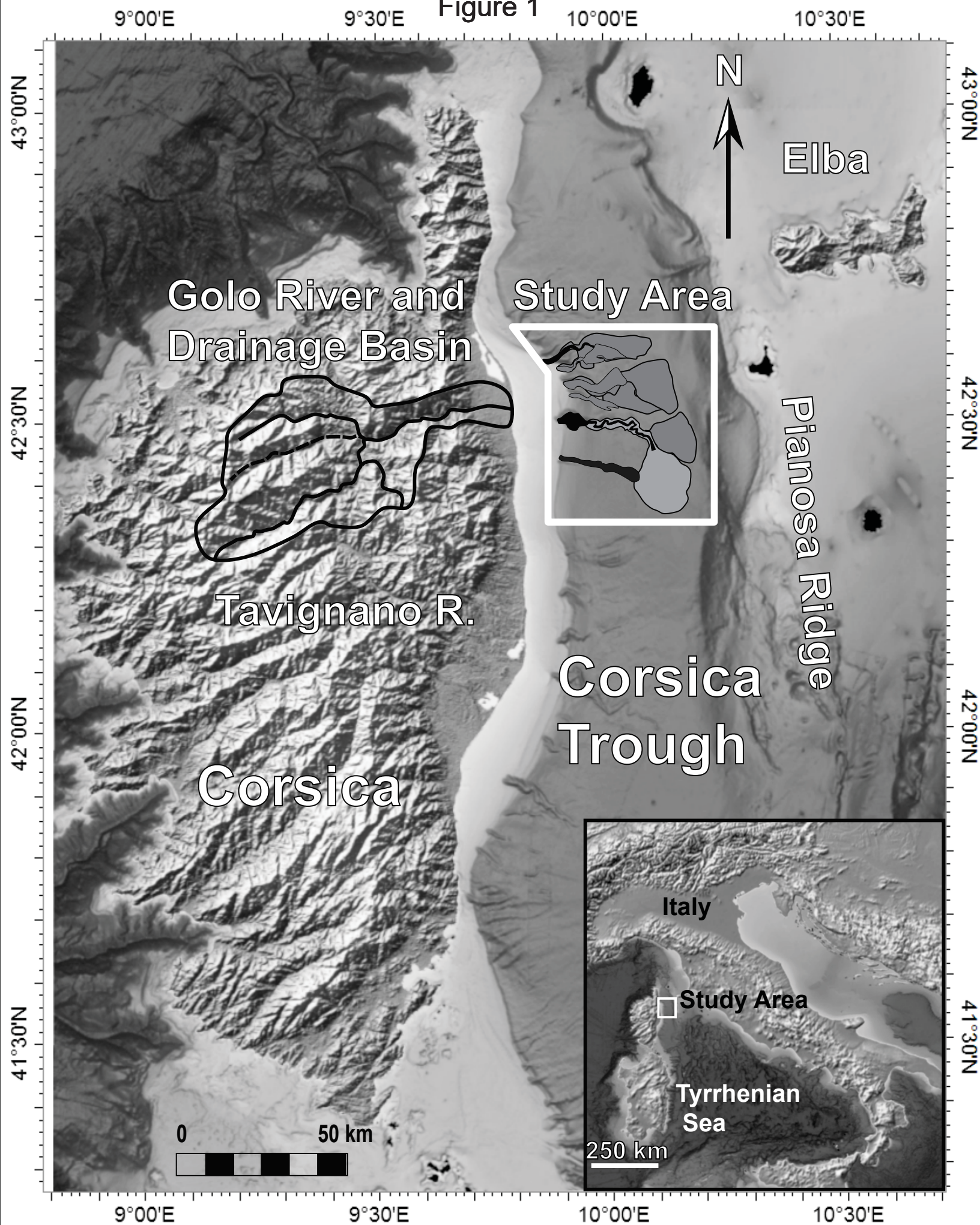
1041 Table 1. Location, length, and sediment recovery of cores used in this study.

1042 Table 2. Sediment volumes, estimated time of deposition and sedimentation rates for the
1043 lowstand systems tract deposit (LS1100, LS1000, etc.) and intervening mud-rich transgressive
1044 and highstand systems tract deposits (TH1100, TH1000 etc.) mapped in the study area. Sand
1045 percent was estimated from core and seismic facies data.

1046

1047

Figure 1



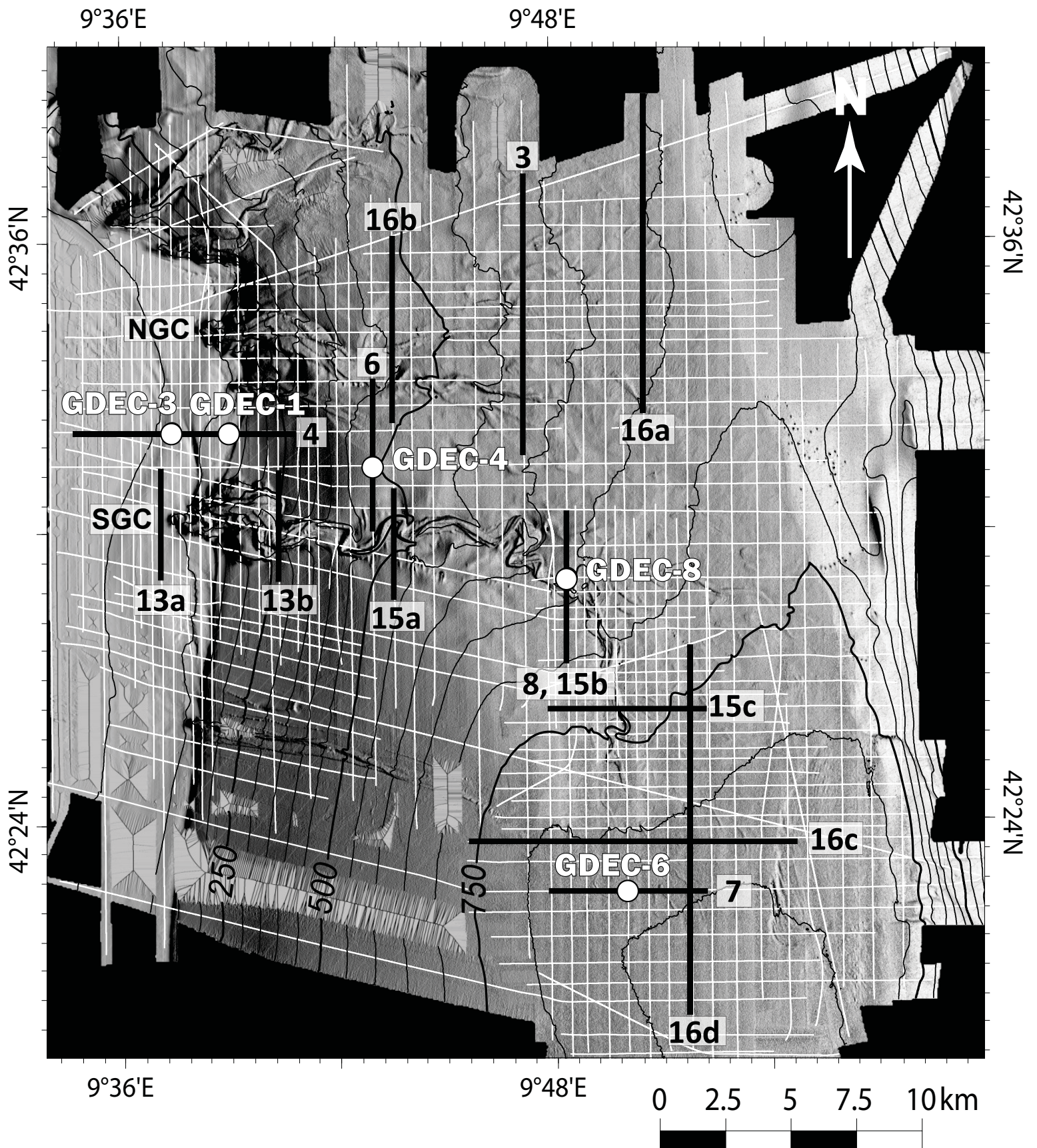
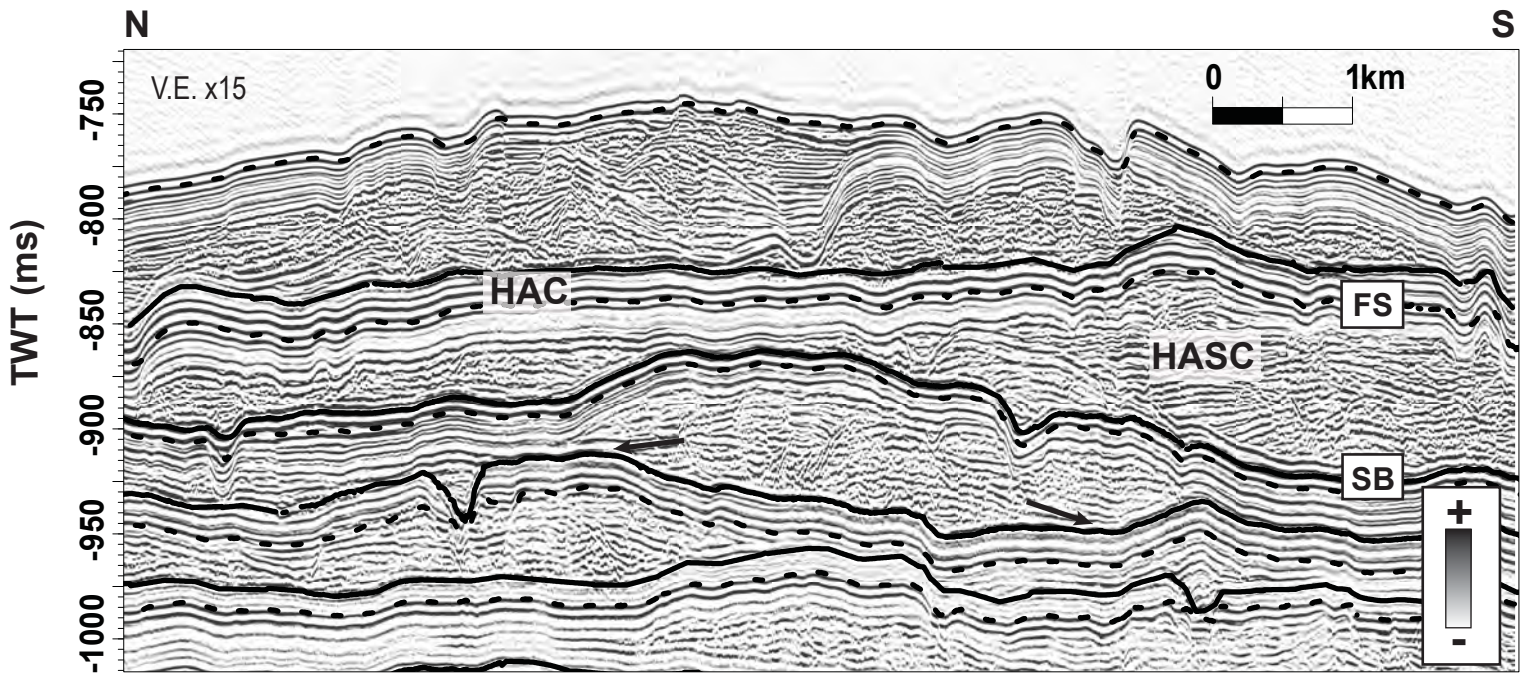


Figure 3

Sweet et al. Figure 3



Sweet et al. Figure 4

Figure 4

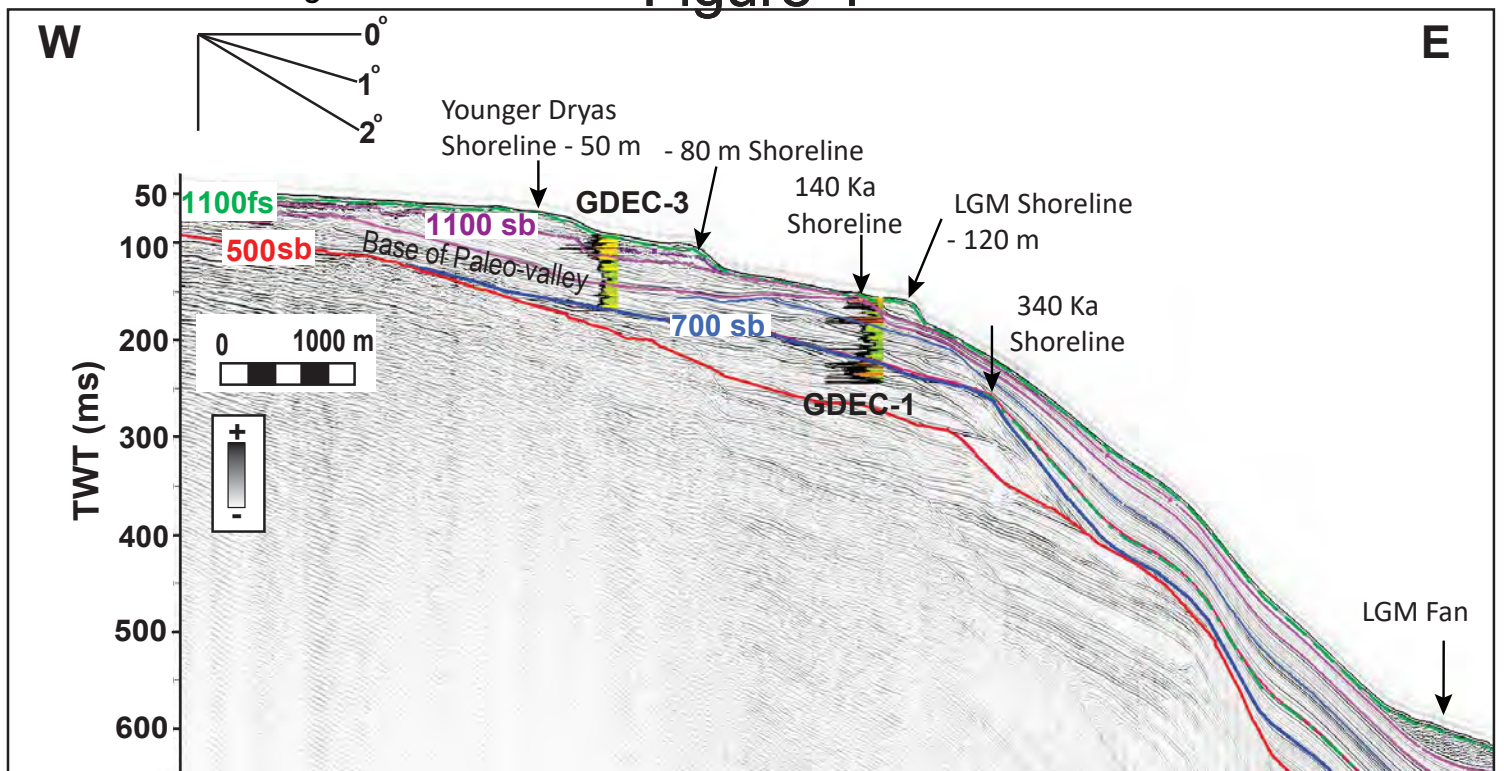


Figure 5

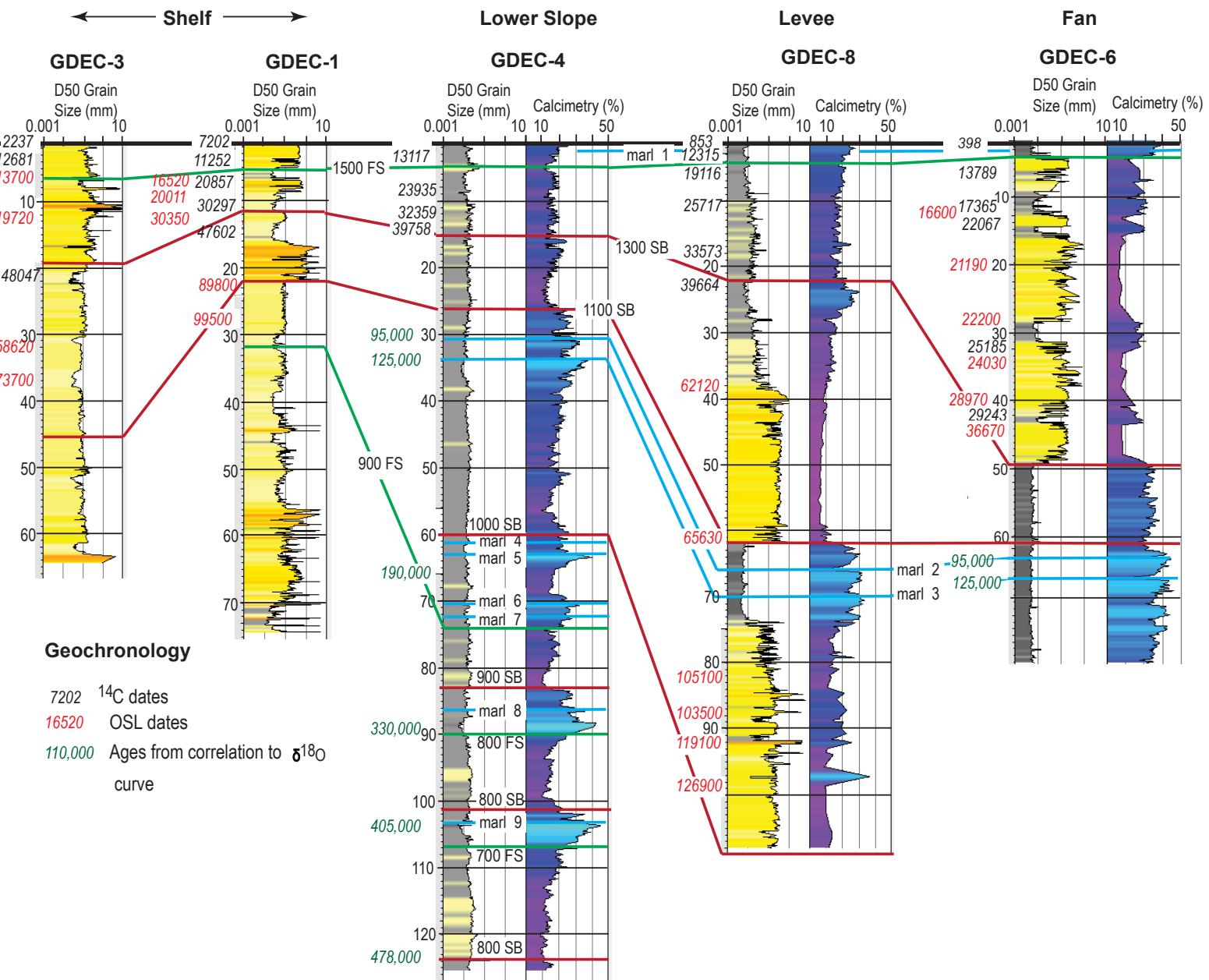


Figure 6

Sweet et al. Figure 6

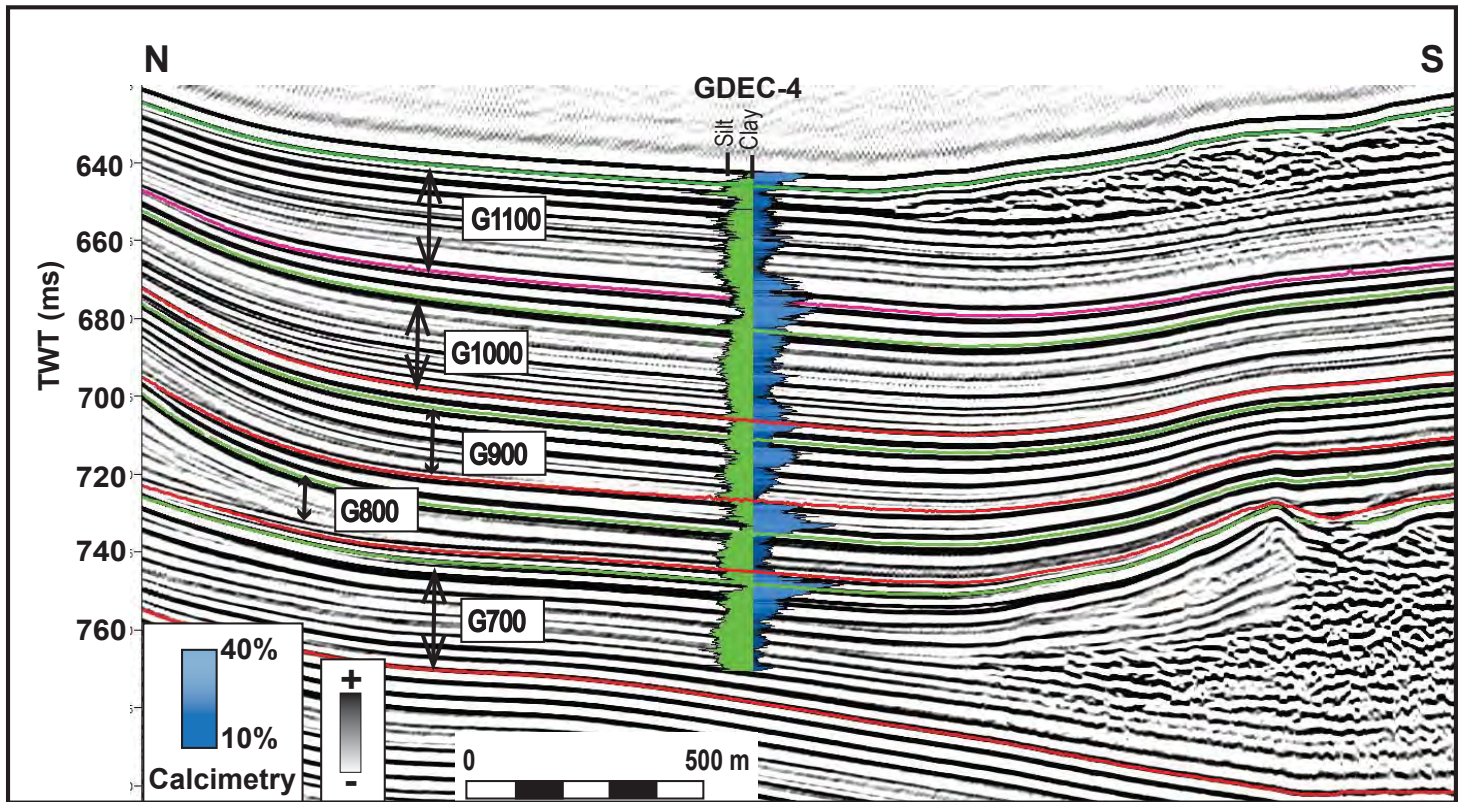


Figure 7

Sweet et al. Figure 7

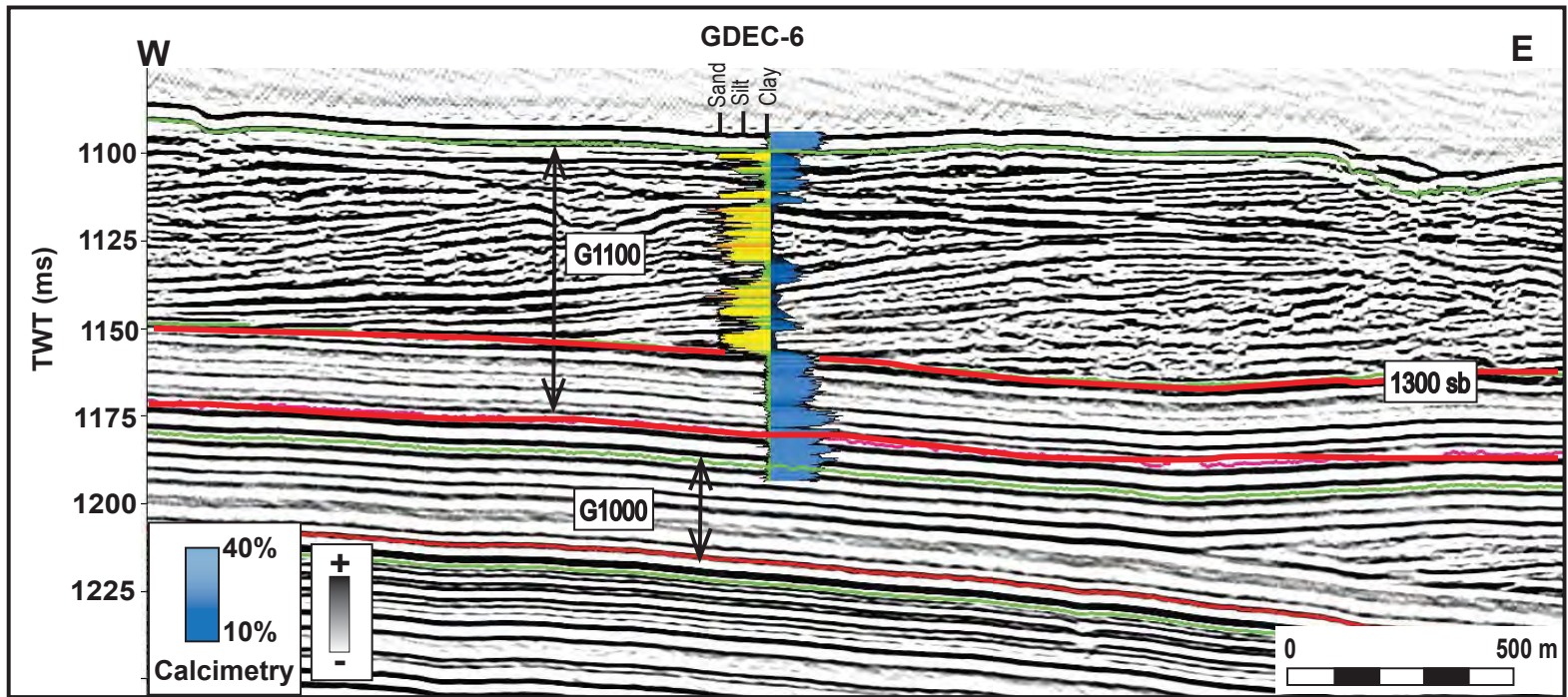
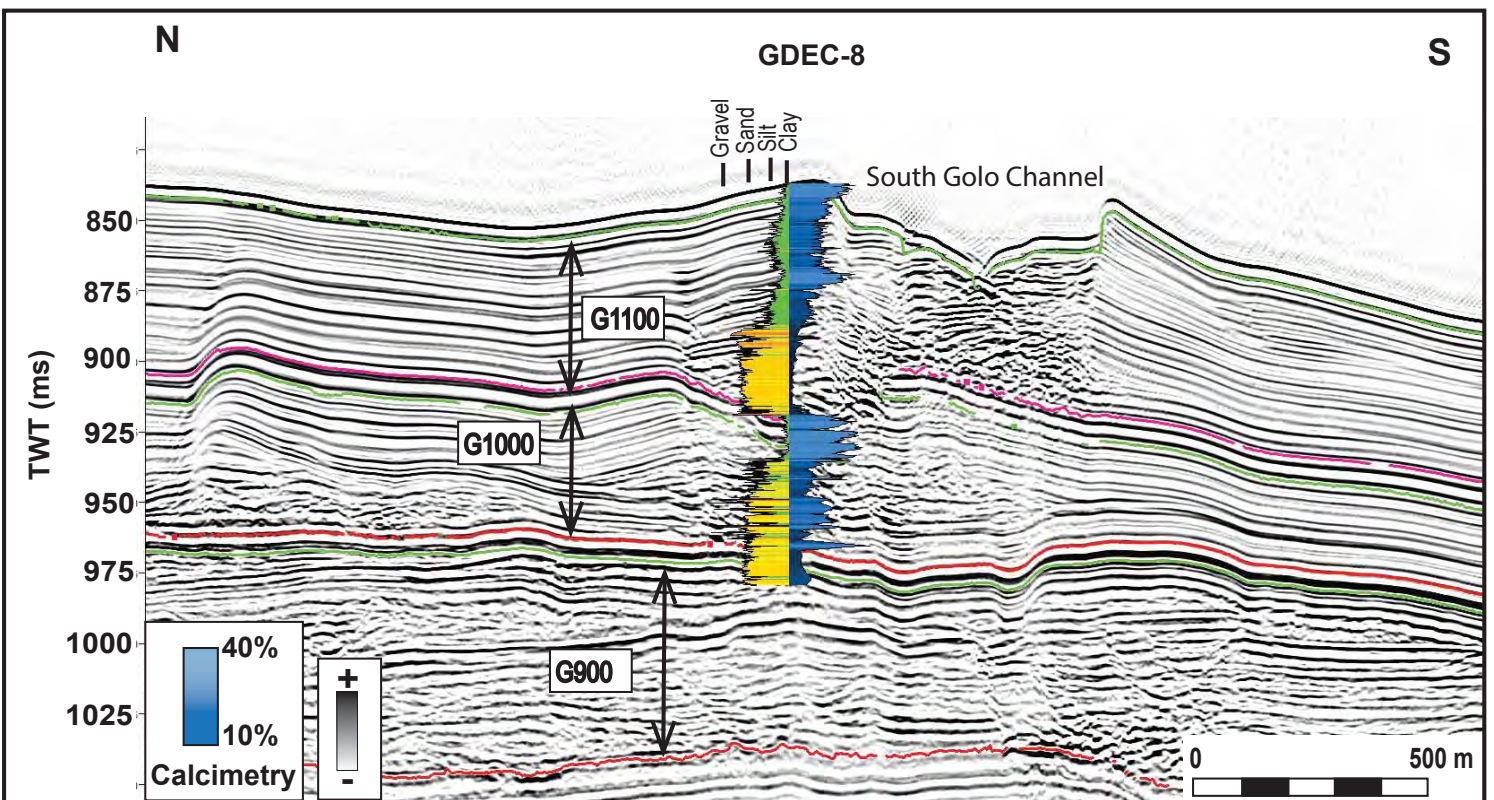


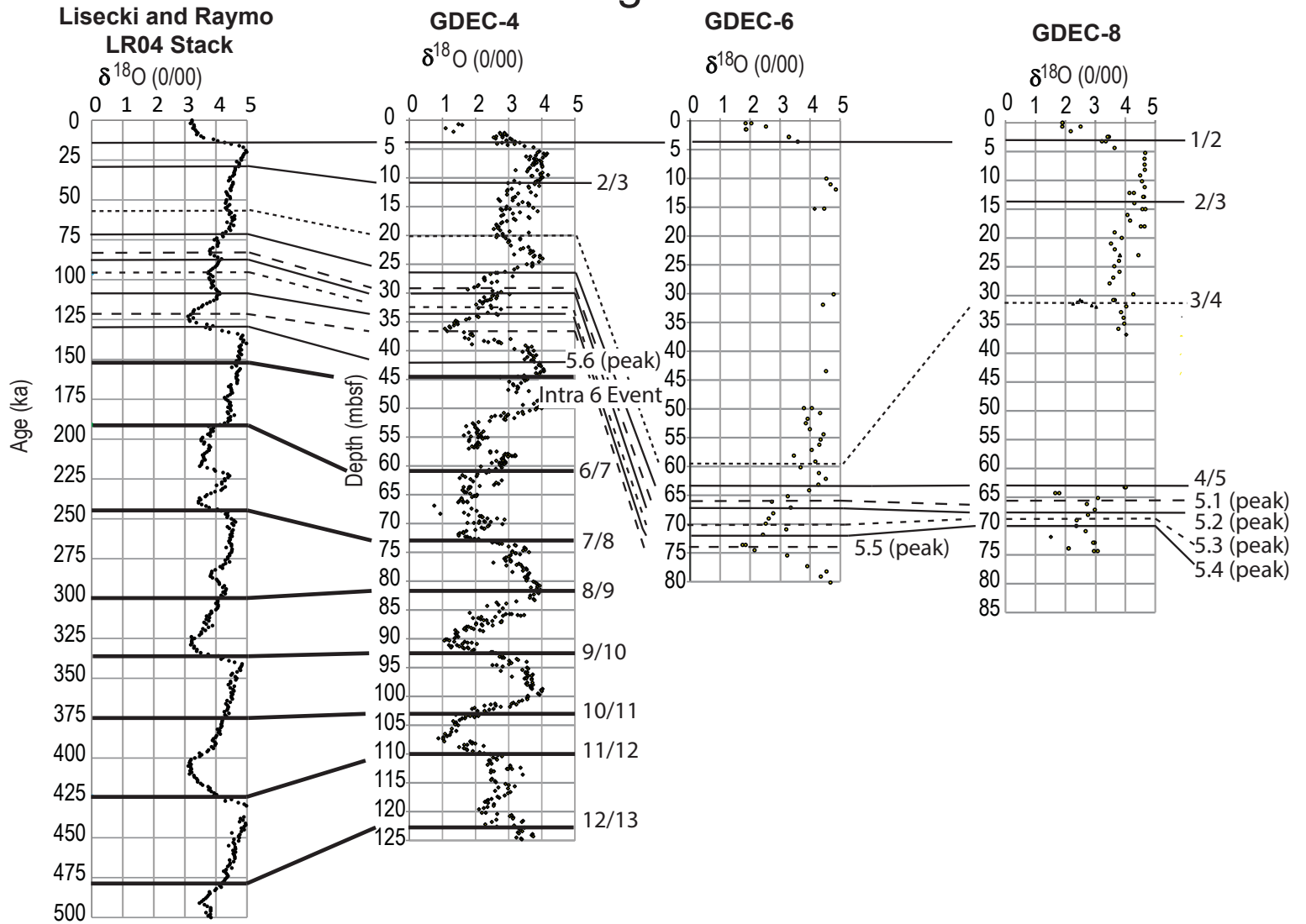
Figure 8

Sweet et al. Figure 8



Sweet et al. Figure 9

Figure 9



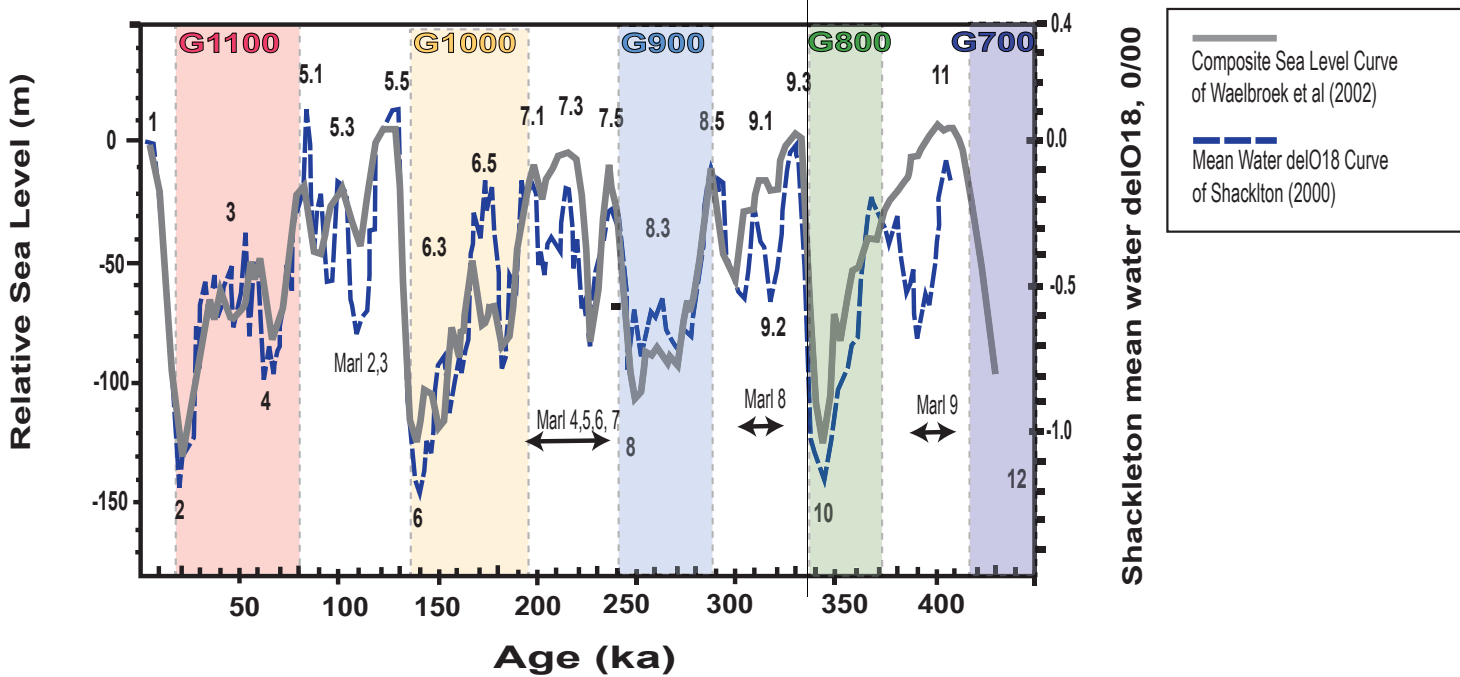
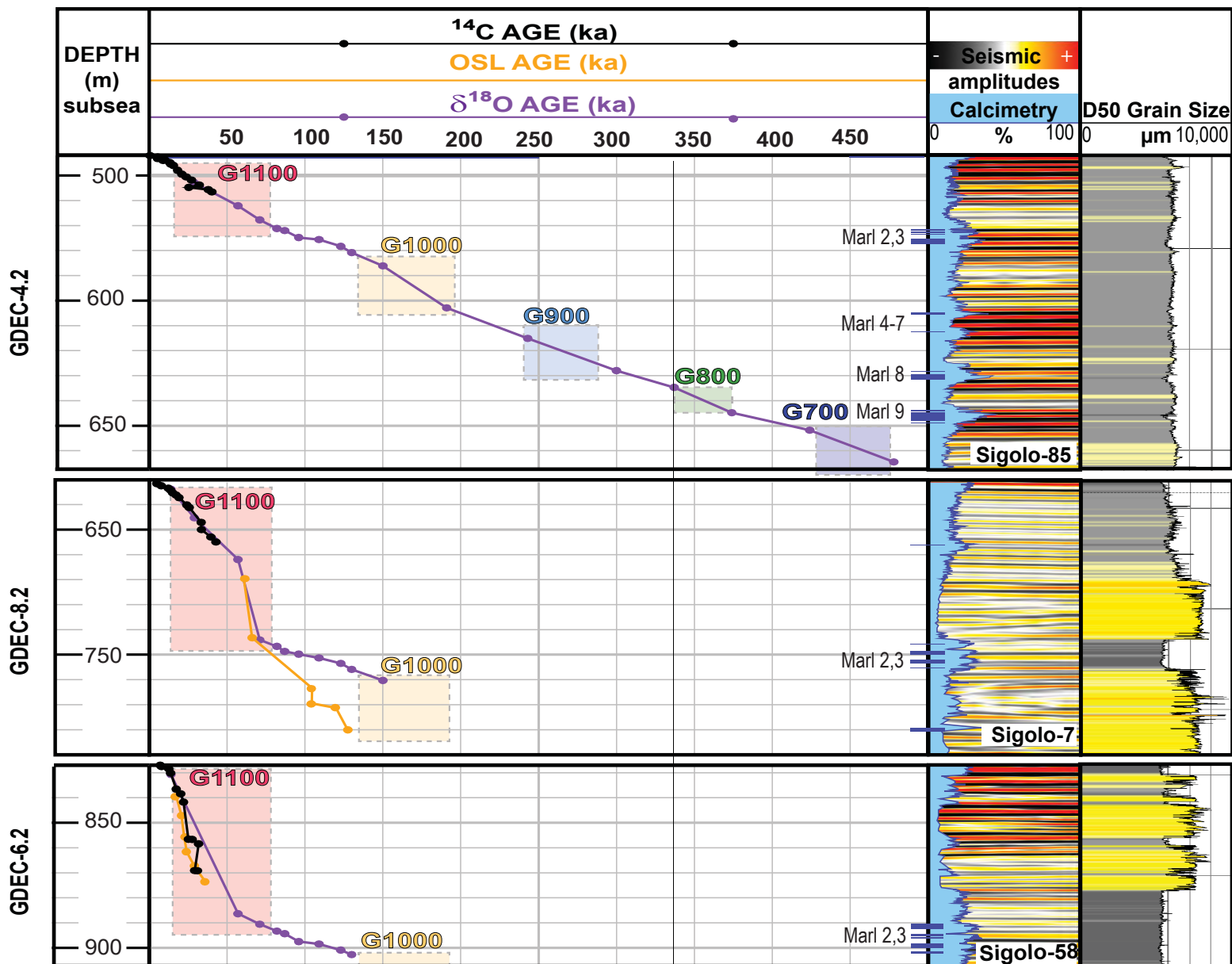
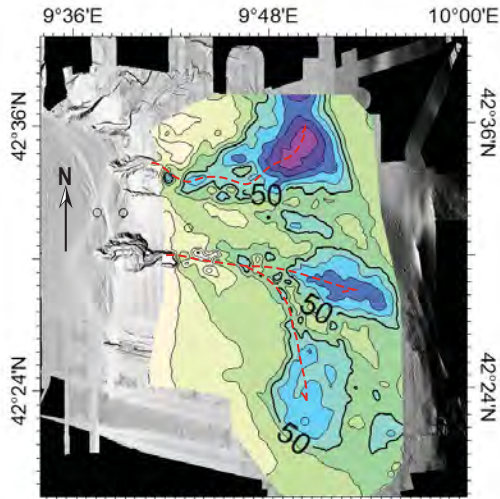
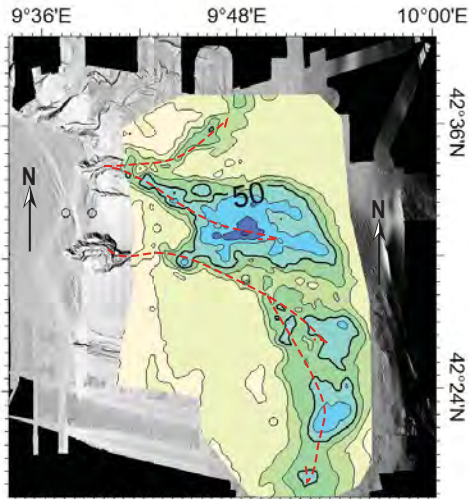


Figure 11

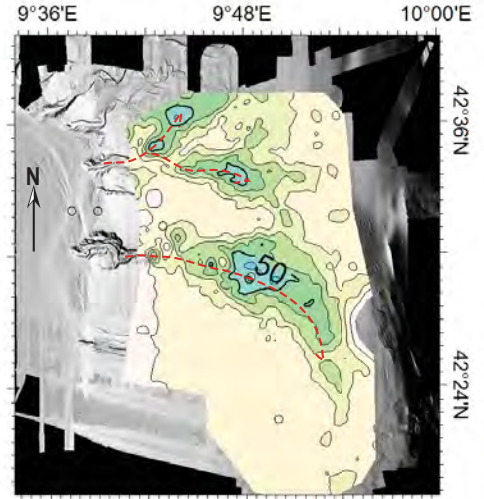
G1100 Sequence (MIS-4 and 2) Fans



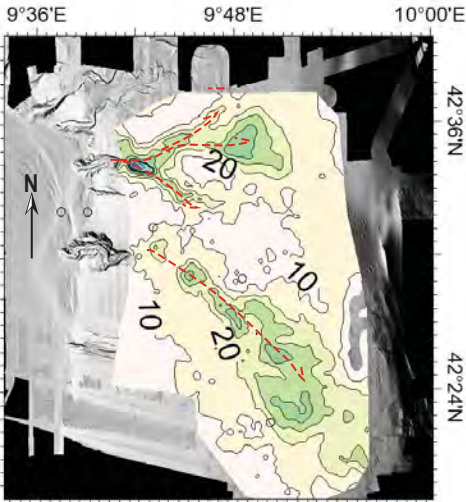
G1000 Sequence (MIS-6) Fans



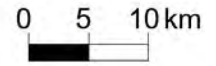
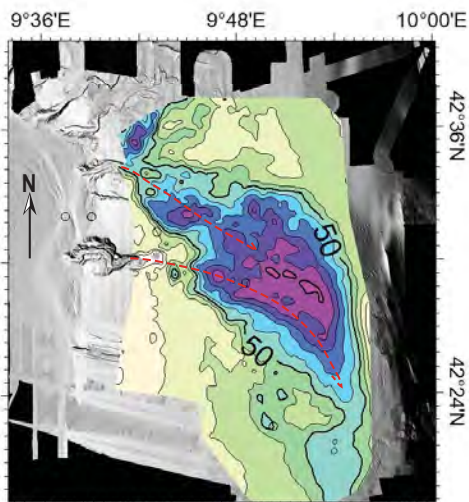
G900 Sequence (MIS-8) Fans



G800 Sequence (MIS-10) Fans



G700 Sequence (MIS-12) Fans



Thickness (m)

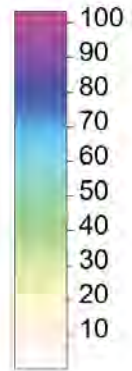


Figure 12

Sweet et al. Figure 12

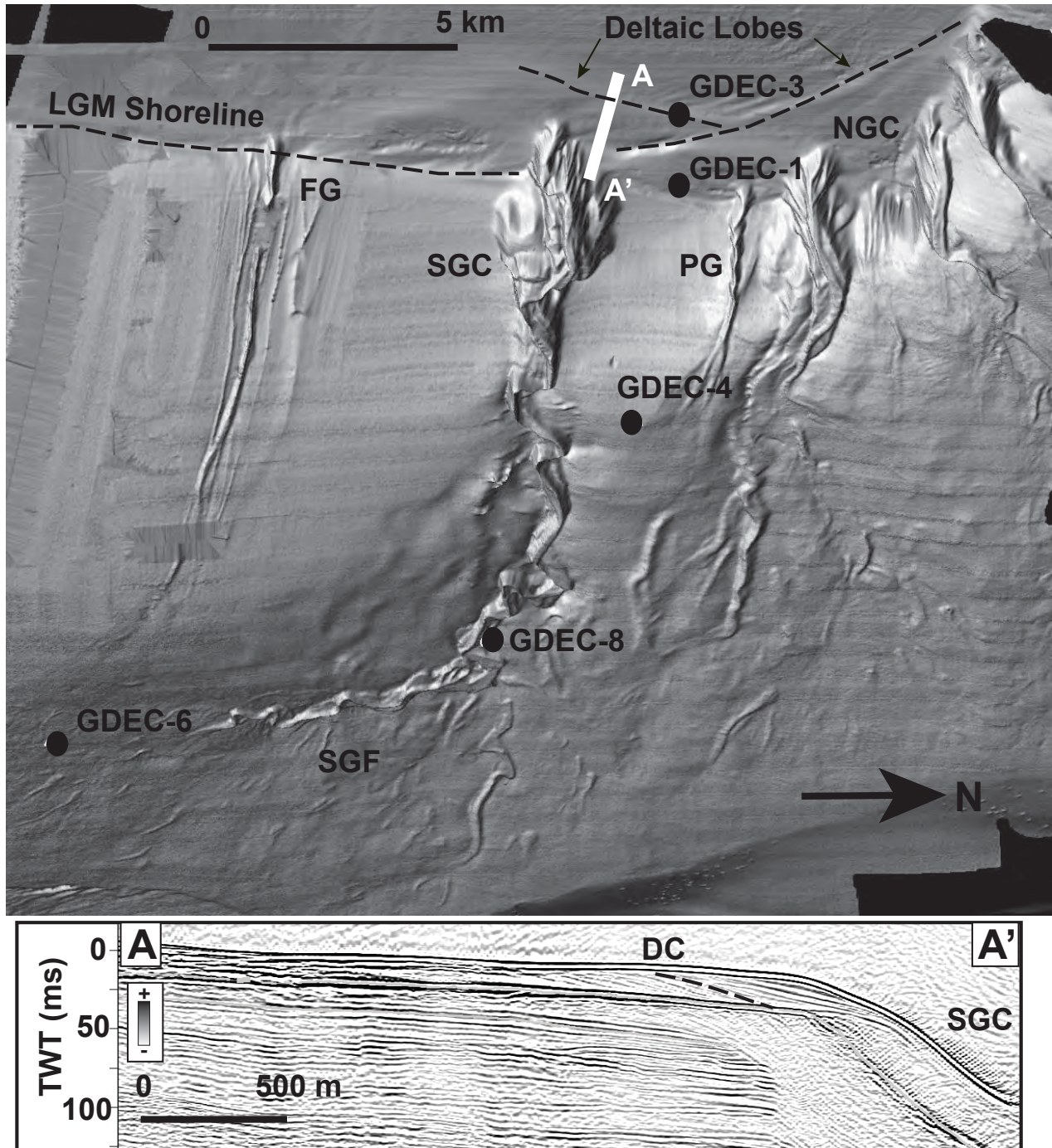


Figure 13

Sweet et al. Figure 13

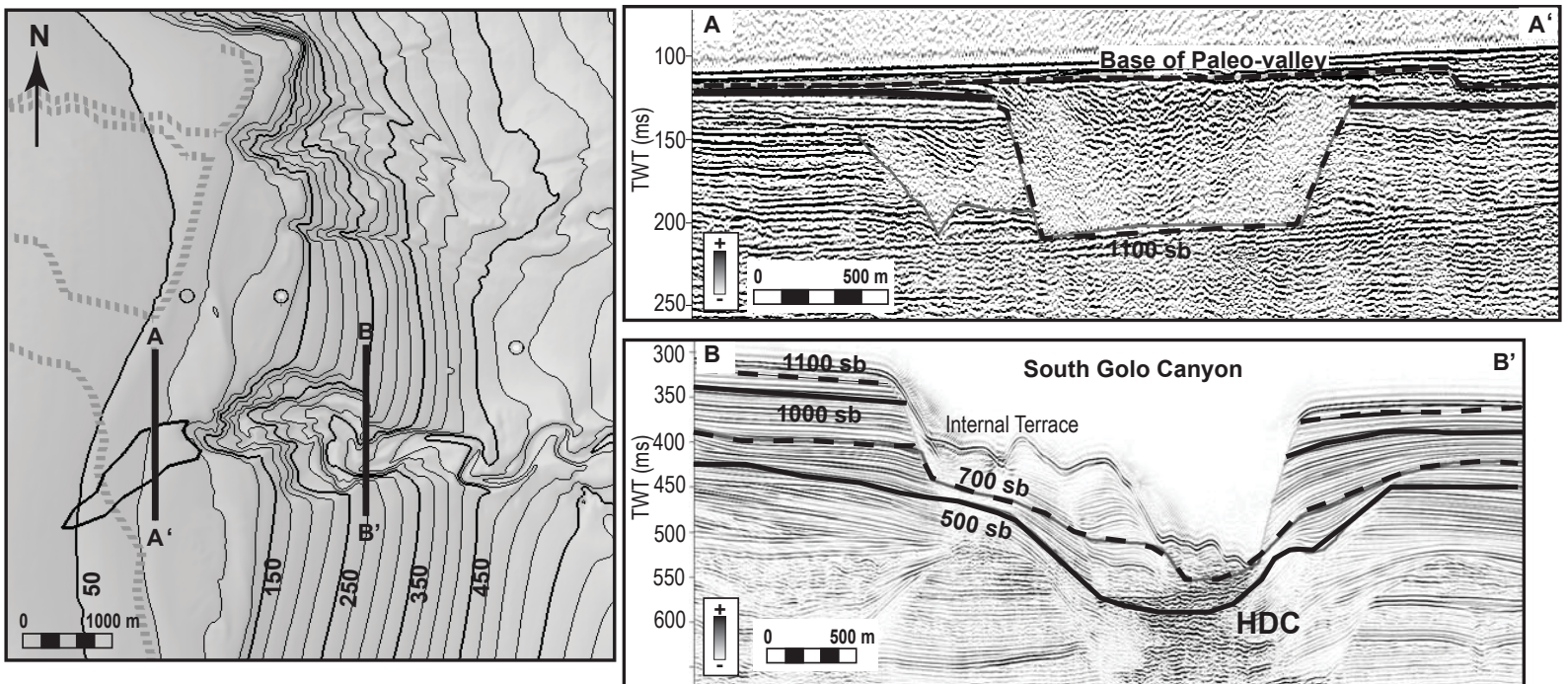


Figure 14

Sweet et al. Figure 14

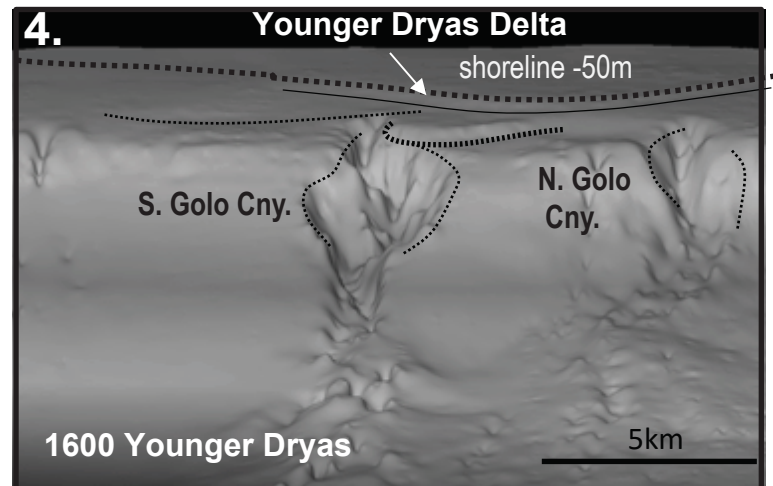
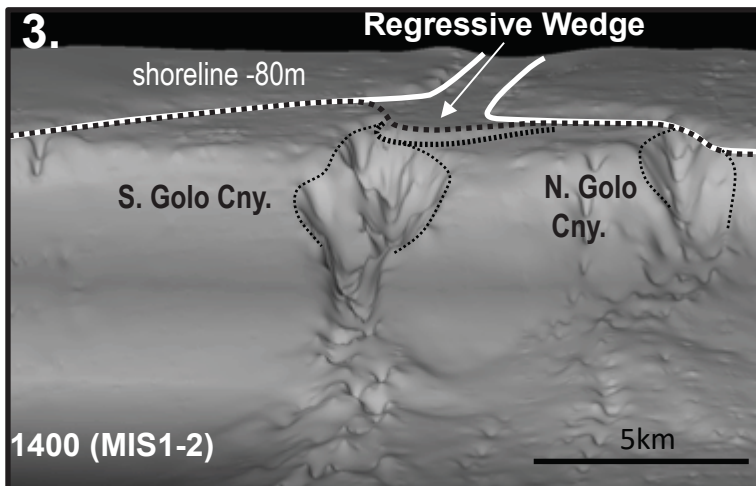
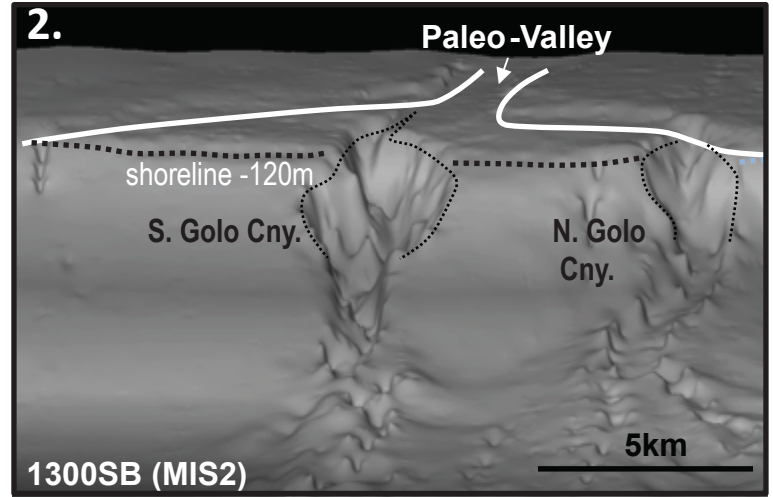
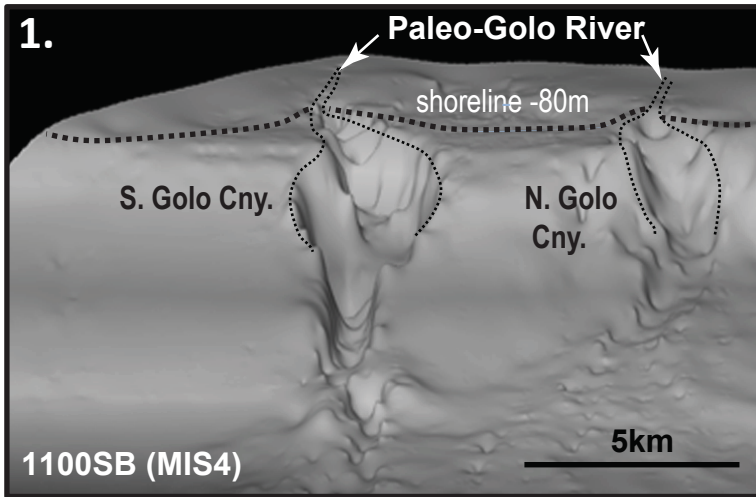


Figure 15

Sweet et al. Figure 15

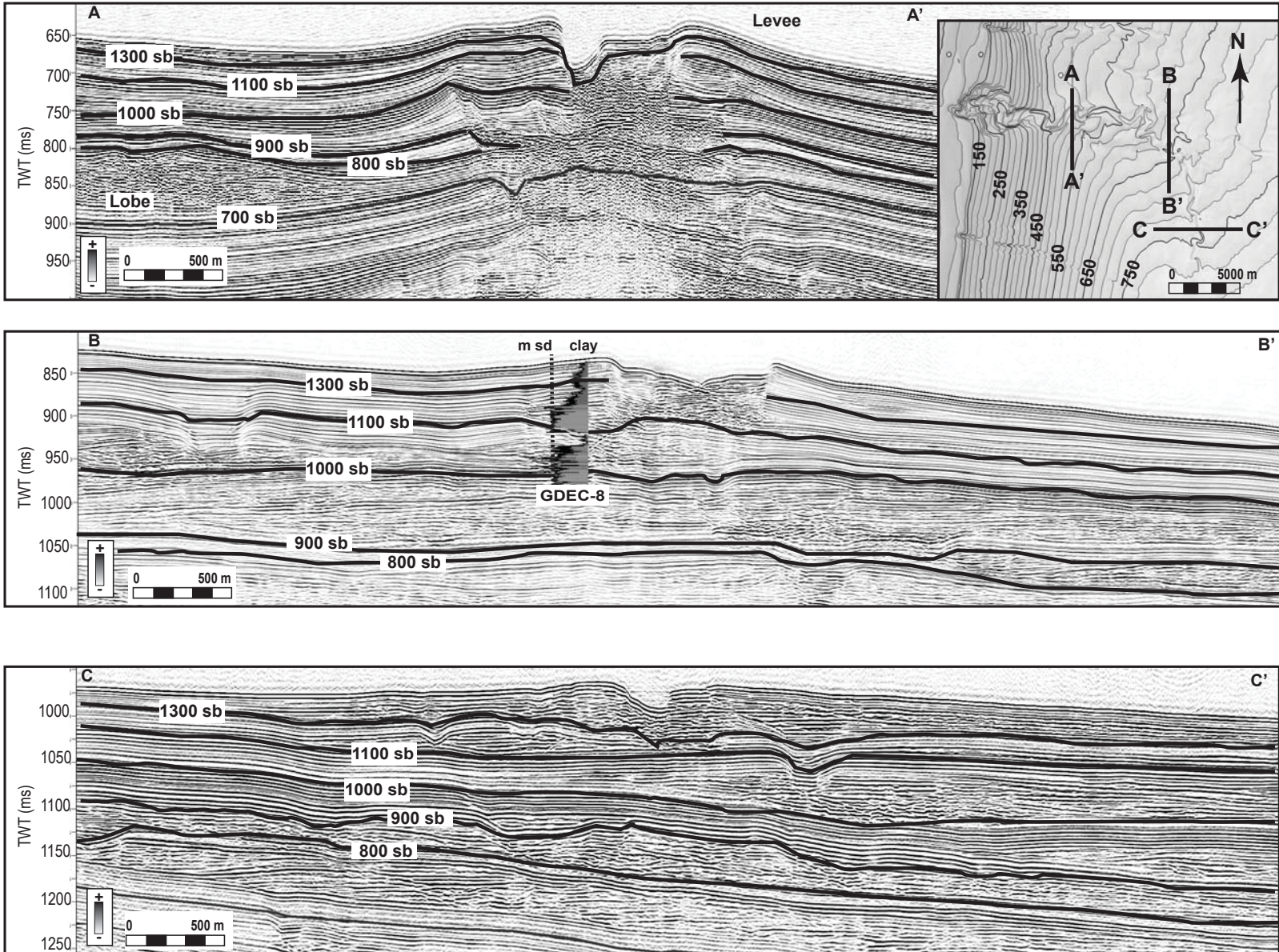


Figure 16

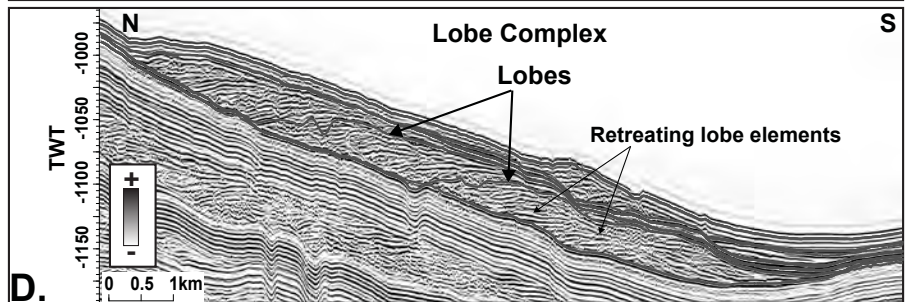
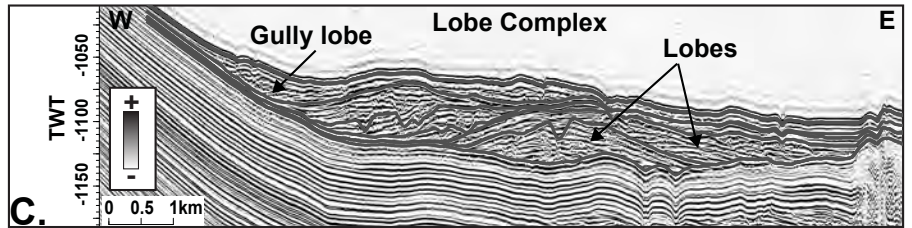
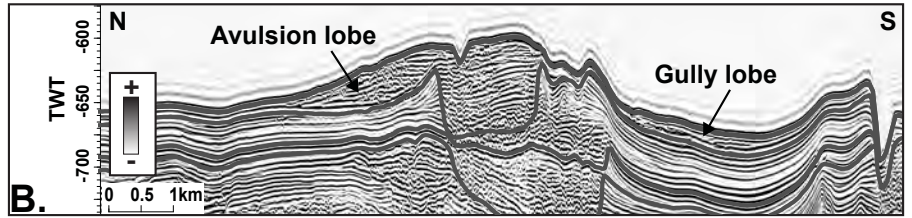
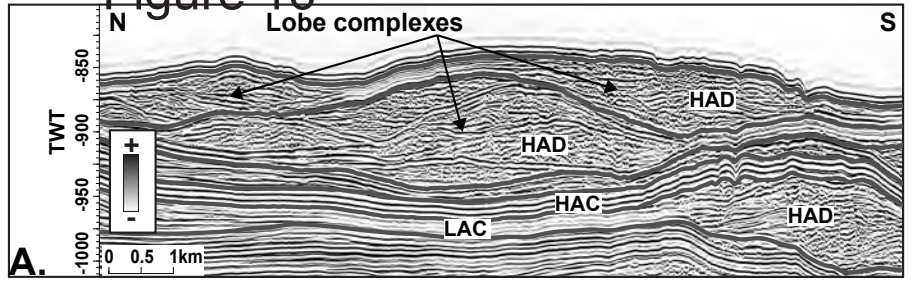
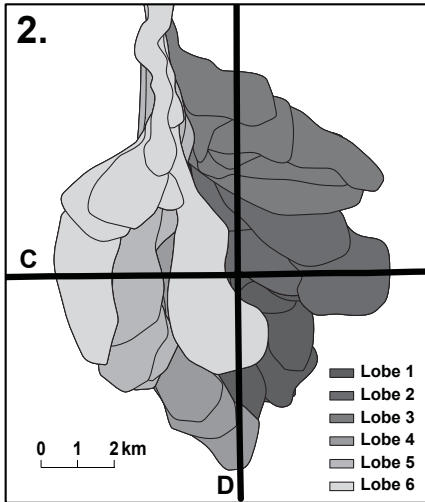
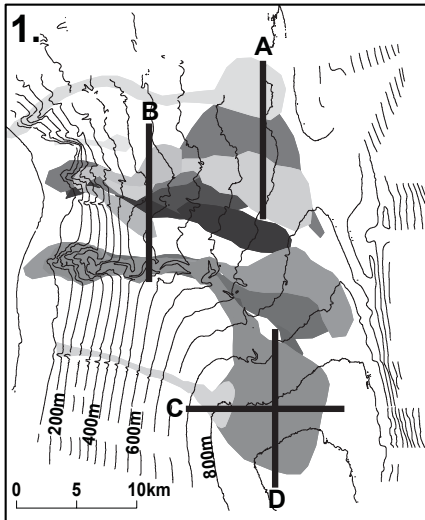
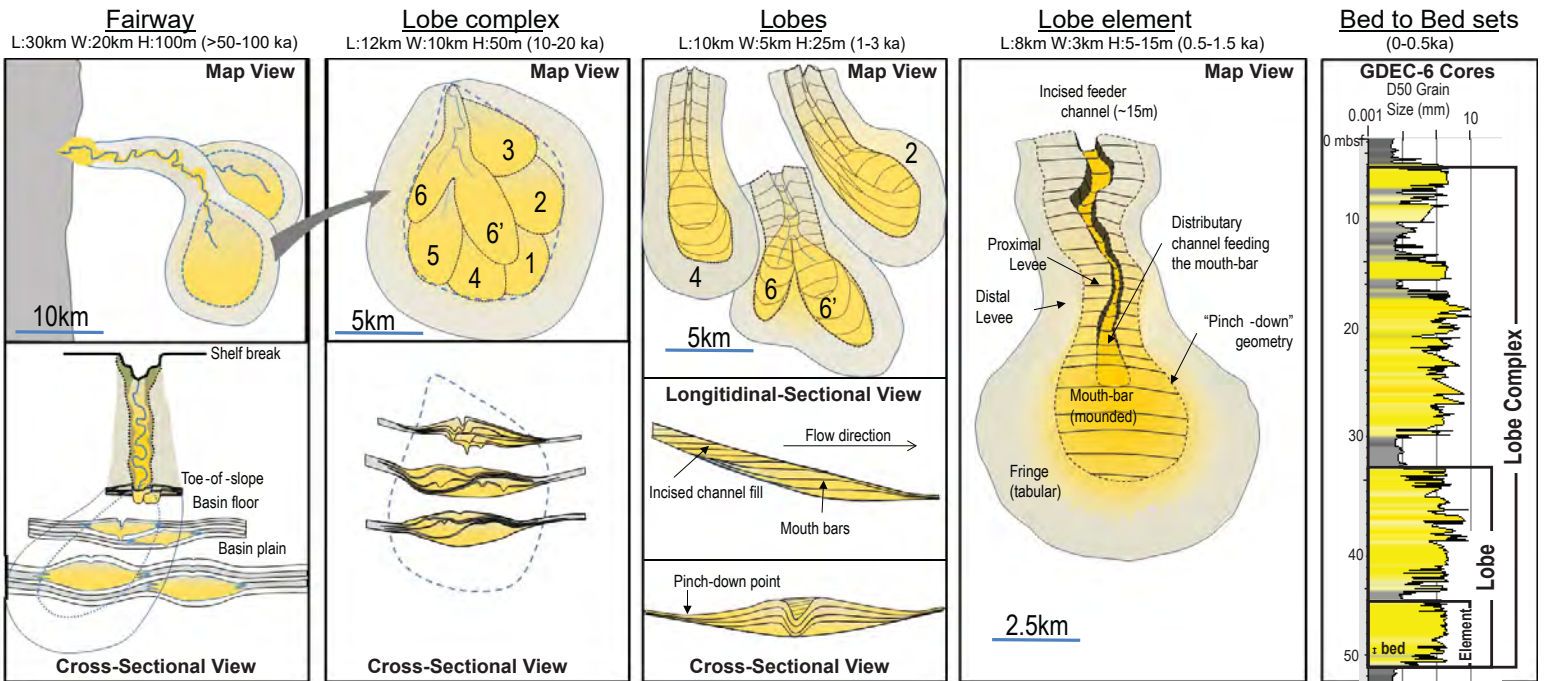


Figure 17



Well	Location	Water Depth (m)	Total Cored Depth (mbsf)	Recovery (%)	Latitude (N)	Longitude (E)
GDEC-1	Shelf	116	75.2	91	42° 32' 05.741	9° 38' 59.990
GDEC-3	Shelf	68	64.8	91	42° 32' 06.661	9° 37' 23.827
GDEC-4	Slope	491	125.7	93	42° 31' 23.243	9° 42' 06.661
GDEC-6	Fan	826	80.2	75	42° 22' 34.876	9° 49' 59.770
GDEC-8	Levee	631	108.8	88	42° 29' 03.173	9° 48' 23.212

Interval	Area (m ²)	Sand (%)	Total Volume (m ³)	Sediment Volume (m ³) (assumes 30% porosity)	Duration (ka)	Average Thickness (m)	Total Rate (m/ka)	Sand Rate (m/ka)	Mud Rate (m/ka)
TH1100	5.87E+08	0	1.92E+09	1.35E+09	0-14	2.29	0.16	0.00	0.16
LS1100	5.87E+08	69	2.54E+10	1.78E+10	14-87	30.29	0.41	0.29	0.13
TH1000	5.87E+08	0	4.37E+09	3.06E+09	87-135	5.21	0.11	0.00	0.11
LS1000	5.87E+08	63	1.91E+10	1.34E+10	135-190	22.78	0.35	0.22	0.13
TH900	5.87E+08	0	2.87E+09	2.01E+09	190-240	3.42	0.07	0.00	0.07
LS900	5.87E+08	47	1.98E+10	1.38E+10	240-290	23.57	0.59	0.28	0.31
TH800	5.87E+08	0	7.07E+09	4.95E+09	290-340	8.44	0.17	0.00	0.17
LS800	5.87E+08	50	1.00E+10	7.03E+09	340-375	11.97	0.34	0.17	0.17
TH700	5.87E+08	0	4.09E+09	2.86E+09	375-415	4.87	0.19	0.00	0.19